

1 **Multi-scale evolution of Kelvin-Helmholtz waves at the Earth's magnetopause during**  
2 **southward IMF periods**

3 T. K. M. Nakamura<sup>1,2</sup>, K. A. Blasl<sup>1,2</sup>, H. Hasegawa<sup>3</sup>, T. Umeda<sup>4</sup>, Y. -H. Liu<sup>5</sup>, S. A. Peery<sup>5</sup>, F.  
4 Plaschke<sup>2,6</sup>, R. Nakamura<sup>2</sup>, J. C. Holmes<sup>2</sup>, J. E. Stawarz<sup>7</sup> and W. D. Nystrom<sup>8</sup>

5  
6 <sup>1</sup>Institute of Physics, University of Graz, Graz 8010, Austria.

7 <sup>2</sup>Space Research Institute, Austrian Academy of Sciences, Graz 8010, Austria.

8 <sup>3</sup>Institute of Space and Astronautical Science, Japan Aerospace Exploration Agency, Sagamihara 252-  
9 5210, Japan.

10 <sup>4</sup>Institute for Space-Earth Environmental Research, Nagoya University, Nagoya 464-8601, Japan

11 <sup>5</sup>Department of Physics and Astronomy, Dartmouth College, Hanover, New Hampshire 03755, USA.

12 <sup>6</sup>Institute of Geophysics and extraterrestrial Physics, TU Braunschweig, Braunschweig 38092, Germany

13 <sup>7</sup>Department of Physics, Imperial College London, London SW7 2BW, UK.

14 <sup>8</sup>HPC division, Los Alamos National Laboratory, Los Alamos, New Mexico 87545, USA.

15 Corresponding author: Takuma Nakamura ([takuma.tkm.nakamura@gmail.com](mailto:takuma.tkm.nakamura@gmail.com))

16 **Abstract**

17 At the Earth's low-latitude magnetopause, the Kelvin-Helmholtz instability (KHI), driven by the  
18 velocity shear between the magnetosheath and magnetosphere, has been frequently observed  
19 during northward interplanetary magnetic field (IMF) periods. However, the signatures of the  
20 KHI have been much less frequently observed during southward IMF periods, and how the KHI  
21 develops under southward IMF has been less explored. Here, we performed a series of realistic  
22 2-D and 3-D fully kinetic simulations of a KH wave event observed by the Magnetospheric  
23 Multiscale (MMS) mission at the dusk-flank magnetopause during southward IMF on September  
24 23, 2017. The simulations demonstrate that the primary KHI bends the magnetopause current  
25 layer and excites the Rayleigh-Taylor instability (RTI), leading to penetration of high-density  
26 arms into the magnetospheric side. This arm penetration disturbs the structures of the vortex  
27 layer and produces intermittent and irregular variations of the surface waves, which significantly  
28 reduces the observational probability of the periodic KH waves. The simulations further  
29 demonstrate that in the non-linear growth phase of the primary KHI, the lower-hybrid drift  
30 instability (LHDI) is induced near the edge of the primary vortices and contributes to an efficient  
31 plasma mixing across the magnetopause. The signatures of the large-scale surface waves by the  
32 KHI/RTI and the small-scale fluctuations by the LHDI are reasonably consistent with the MMS  
33 observations. These results indicate that the multi-scale evolution of the magnetopause KH  
34 waves and the resulting plasma transport and mixing as seen in the simulations may occur during  
35 southward IMF.

## 36 I. INTRODUCTION

37 The Kelvin-Helmholtz instability (KHI) becomes unstable when the plasma shear flow is  
38 super-Alfvénic for the magnetic field component parallel to the shear flow (Chandrasekhar,  
39 1961). This unstable condition is easily satisfied when the magnetic field is oriented nearly  
40 perpendicular to the direction of the shear flow. At the Earth's low-latitude magnetopause, this  
41 magnetic field configuration appears when the interplanetary magnetic field (IMF) is strongly  
42 northward or southward. Indeed, clear signatures of surface waves and flow vortices, which  
43 could be generated by the KHI, have been frequently observed around the low-latitude  
44 magnetopause during periods of strong northward IMF (e.g., Sckopke et al., 1981; Kokubun et  
45 al., 1994; Slinker et al., 2003; Kivelson & Chen, 1995; Fairfield et al., 2000; Hasegawa et al.,  
46 2004, 2006; Foullon et al., 2008; Kavosi & Raeder, 2015; Moore et al., 2016). These  
47 magnetopause KH waves and vortices have been believed to cause efficient mass, momentum  
48 and energy transfer across the magnetopause and effectively contribute to forming the Earth's  
49 low-latitude boundary layer (LLBL), where plasmas of magnetosheath and magnetospheric  
50 origins are mixed, during the northward IMF periods (e.g., Nakamura, 2021 and references  
51 therein).

52 On the other hand, although the magnetopause boundary layer can be unstable for the  
53 KHI even for the southward IMF in the MHD regime as long as the magnetic field component  
54 parallel to the shear flow is weak enough (Chandrasekhar, 1961), the signatures of the  
55 magnetopause KH waves and vortices have been much less frequently observed during periods  
56 of southward IMF (e.g., Kavosi & Raeder, 2015). Hwang et al. (2011) reported a Cluster  
57 observation event of non-linear KH vortices during a southward IMF period. In this event,  
58 observed plasma and field variations were irregular and temporally intermittent, indicating that  
59 the structure of the KH vortices was being disturbed. A recent 3-D fully kinetic simulation under  
60 pure southward IMF conditions demonstrated that strong evolution of magnetic reconnection  
61 across thin current layers formed within the KH waves quickly destroys the wave and vortex  
62 structures (Nakamura et al., 2020a). This reconnection-driven decay process of the KH vortex  
63 may explain the intermittent and irregular variations of the observed KH vortices as well as the  
64 low observational probability of the periodic KH waves/vortices during southward IMF.  
65 However, it was difficult to resolve the thin current layers and confirm the occurrence of the

This is the author's peer reviewed, accepted manuscript. However, the online version of record will be different from this version once it has been copyedited and typeset.

PLEASE CITE THIS ARTICLE AS DOI: 10.1063/1.50067391

Manuscript submitted to Physics of Plasmas

66 vortex-induced reconnection (VIR) in the reported Cluster event because of the insufficient time  
67 resolution in plasma measurements.

68 High-time-resolution fields and plasma data collected by the Magnetospheric Multiscale  
69 (MMS) mission (Burch et al., 2016) have been used to resolve small-scale physics within the KH  
70 waves and vortices such as the VIR, as recently shown for some magnetopause KH wave events  
71 during the northward IMF (Eriksson et al., 2016a,b; Li et al., 2016; Vernisse et al., 2016;  
72 Stawarz et al., 2016; Tang et al., 2018; Hasegawa et al., 2020; Hwang et al., 2020; Kieokaew et  
73 al., 2020). In these northward IMF events, signatures of the VIR such as reconnection outflow  
74 jets (Eriksson et al., 2016a; Li et al., 2016), energy dissipation within the electron diffusion  
75 region (Eriksson et al., 2016b), turbulent spectra caused by turbulent evolution of the VIR  
76 (Stawarz et al., 2016; Hasegawa et al., 2020), and the formation of multiple flux ropes and their  
77 interactions (Hwang et al. 2020; Kieokaew et al., 2020) were reported. 3-D fully kinetic  
78 simulations of one of these MMS events on September 8, 2015 showed that the simulated VIR  
79 signatures are reasonably consistent with many of the above observation signatures (Nakamura et  
80 al., 2017a,b, Nakamura et al., 2020b, Nakamura, 2021). Although past theoretical and numerical  
81 studies suggested that the plasma shear flow can reduce the rate of spontaneous reconnection and  
82 weaken the resulting solar wind transport across the magnetopause (e.g., Cassak and Otto, 2011),  
83 these realistic simulations of the observed VIR further showed that the VIR, which is a strongly  
84 driven reconnection process controlled by the super-Alfvénic vortex flow and whose rate is  
85 much higher than that of spontaneous reconnection, leads to an efficient solar wind transport.  
86 Based on the consistencies between the observations and simulations, these studies indicated that  
87 the KHI and subsequent occurrence of the VIR would indeed contribute to efficient solar wind  
88 transport during northward IMF.

89 Based on these previous studies, our companion paper, Blasl et al. (accepted; hereafter  
90 referred to as B21), reported the first MMS observations of the KH waves during southward  
91 IMF. In this event, MMS observed the intermittent and irregular variations of the surface waves,  
92 which can be interpreted as being formed by the KHI, during the southward IMF and  
93 magnetosheath magnetic field. Although clear VIR signatures as reported in the above MMS  
94 observation events for the northward IMF were not found in this event, the high-time-resolution  
95 measurements of MMS frequently detected small-scale fluctuations, which can be interpreted as  
96 being generated by the lower-hybrid drift instability (LHDI), excited near the edge of the surface

97 waves. To investigate this event in more detail, in the present paper, we perform a series of 2-D  
98 and 3-D fully kinetic simulations with parameters matched to this MMS event. The simulation  
99 results are consistent with the observations in terms of both large-scale surface wave signatures  
100 and small-scale LHDI fluctuations. The simulations also demonstrate that the primary KH waves  
101 induce the secondary Rayleigh-Taylor instability (RTI) at the surface bent by the KHI. The RTI  
102 forms high-density arms penetrating into the low-density magnetospheric side. This arm  
103 penetration quickly disturbs the primary KH wave structures and produces intermittent and  
104 irregular variations of the surface waves, leading to a reduction in the observational probability  
105 of the primary KH waves. Interestingly, this RTI-related reduction of the observational  
106 probability of the KH waves proceeds faster than the above VIR-related reduction for the  
107 northward IMF, indicating that the secondary RTI may also be a key process that makes it more  
108 difficult to detect the KH waves during southward IMF.

109 This paper is organized as follows. Sec. II describes the details of the simulation model  
110 employed in this paper. Sec. III presents the overall simulation results focusing on the large-scale  
111 variations of the surface waves, while in Sec. IV we focus on the secondary processes induced  
112 within the primary waves. In Sec. V, we summarize the results and discuss differences in the  
113 evolution of the KH waves between the northward and southward IMF conditions.

114

## 115 II. MODEL

### 116 A. Simulation settings

117 We performed a series of 2-D (in the  $x$ - $y$  plane) and 3-D fully kinetic simulations that  
118 model a magnetopause crossing event observed by MMS on September 23, 2017 (B21), using  
119 the high-performance particle-in-cell code VPIC (Bowers et al., 2008, 2009). The  $x$ ,  $y$  and  $z$   
120 coordinates in the simulations correspond to the direction along the velocity shear ( $\sim$ the  
121 magnetosheath flow in the equatorial plane), the boundary normal ( $\sim$ magnetosheath-to-  
122 magnetosphere), and the out-of-the-vortex-plane ( $\sim$ south-to-north), respectively. The initial  
123 density, magnetic field and ion (and electron) bulk velocities across the magnetopause boundary  
124 layer are set to the values obtained from the observations near the KH vortex-like interval 15:33-  
125 15:35 UT (see B21 for more details of this interval). Denoting the magnetosheath and



126 magnetospheric sides as 1 and 2, respectively, we first select the density ( $n_{10}$ ,  $n_{20}$ ), the magnetic  
 127 field ( $B_{x10}$ ,  $B_{z10}$ ,  $B_{x20}$ ,  $B_{z20}$ ), and the bulk velocities ( $U_{x10}$ ,  $U_{z10}$ ,  $U_{x20}$ ,  $U_{z20}$ ) on the two sides from  
 128 the observations. To set the initial equilibrium, we here neglect the y-component of the initial  
 129 magnetic field and velocities, which are negligibly small compared to the x and z components.  
 130 We then set the initial density profiles by connecting these values across the magnetopause using  
 131 a  $\tanh(y/L_0)$  function (Nakamura and Daughton, 2014) as  $n_1(y) = \frac{n_{10}}{2} \left[ 1 - \tanh\left(\frac{z}{L_0}\right) \right]$  and  
 132  $n_2(y) = \frac{n_{20}}{2} \left[ 1 + \tanh\left(\frac{z}{L_0}\right) \right]$ , where  $L_0=2.5d_i$  is the initial half thickness of the shear layer and  
 133  $d_i=c/\omega_{pi}$  is the ion inertial length based on  $n_0=n_{10}$ . To set the bulk velocities, particles (ions and  
 134 electrons) are initialized with drifting Maxwellian velocities whose drift velocities are  $U_{x10}$  and  
 135  $U_{x20}$  for the magnetosheath and magnetospheric particles, respectively. The initial magnetic field  
 136 is set up as  $B_{x,z}(y) = \frac{B_{x,z10}}{2} \left[ 1 - \tanh\left(\frac{y}{L_0}\right) \right] + \frac{B_{x,z20}}{2} \left[ 1 + \tanh\left(\frac{y}{L_0}\right) \right]$ . Additional electron and ion  
 137 flows and electron density are introduced to satisfy the Harris type variation of  $B_x$  and  $B_z$ . To  
 138 satisfy the force balance, the temperatures for the magnetospheric ion and electron components  
 139  $T_{i,e20}$  are set to be higher than the magnetosheath components  $T_{i,e10}$ , where the ion-to-electron  
 140 temperature ratio is fixed as  $T_{i0}/T_{e0}=5.0$ .

141 The set of values obtained from MMS data in regions 1 and 2 are  $n_{10}/n_{20}=8.0$ ,  $B_{z10}=-B_0$ ,  
 142  $B_{z20}=B_0$ ,  $U_{x10}=V_0/2$ , and  $U_{x20}=-V_0/2$ , where  $n_{10}=8\text{cm}^{-3}$ ,  $B_0=12\text{nT}$ ,  $|V_0|=290\text{km/s}=3.0V_A$  ( $V_A$ :  
 143 Alfvén speed based on  $n_0$  and  $B_0$ ). Note that the system is set to be in a drifting frame of  
 144 reference with half the velocity of the magnetosheath flow. Since the in-plane magnetic field  
 145 components ( $B_{x10}$  and  $B_{x20}$ ) are known to easily change within the vortex layer as a result of the  
 146 vortex motion (e.g., Fairfield et al., 2007; Nakamura et al., 2008), it is difficult to determine  $B_{x10}$   
 147 and  $B_{x20}$  from the observations during the vortex-like fluctuating interval. Nevertheless, since the  
 148 spacecraft crossed a relatively steady magnetosheath-like interval just before the vortex-like  
 149 interval, we took  $B_{x10}$  from this interval as  $0.17\text{-}0.2B_0$ . Regarding  $B_{x20}$ , since the spacecraft did  
 150 not cross a clear magnetosphere-like region near the vortex-like interval, we tested various  
 151 values from 0 to  $0.2B_0$ . In this paper, we show representative simulation runs with ( $B_{x10}$ ,  
 152  $B_{x20}$ )=( $0.2B_0$ , 0) and ( $0.17B_0$ ,  $0.17B_0$ ) (i.e., a case with no in-plane field on the magnetospheric  
 153 side and a case with uniform in-plane field) as listed in TABLE I. The total plasma beta on the  
 154 magnetosheath side is  $\beta_1=1.5$ , the ratio between the electron plasma frequency and the

155 gyrofrequency is  $\omega_{pe}/\Omega_e=2.0$  and the ion-to-electron mass ratio is  $m_i/m_e=100$  for all runs. The  
 156 system is periodic in  $x$  (and in  $z$  for 3-D), and  $y$  boundaries are modeled as perfect conductors for  
 157 the fields and reflecting for the particles.

158 In the following sections, we will show the results from 4 runs listed in TABLE I. We  
 159 will first show a large-scale 2-D run (Run-A), in which the system size is  $L_x \times L_y = 100d_i \times 100d_i$   
 160  $= 6144 \times 6144$  cells with a total of  $1.5 \times 10^{10}$  (super)particles. In this run, we added no specific  
 161 mode of initial perturbations and the KH instability grows from the random particle noises. Then,  
 162 to investigate the three-dimensional effects, we will show local 3-D (Run-B) and 2-D (Run-C)  
 163 runs, which feature one wavelength KH mode ( $m_x=1$ ) with the system size  $L_x \times L_y \times L_z$   
 164  $= 15d_i \times 30d_i \times 10.4d_i = 864 \times 1728 \times 600$  cells with a total of  $3.6 \times 10^{11}$  particles for 3-D, and  
 165  $L_x \times L_y = 15d_i \times 30d_i = 864 \times 1728$  cells with a total of  $6.0 \times 10^9$  particles for 2-D. In these local runs, to  
 166 initiate the one wavelength KH mode, we added an initial weak flow perturbation as  $\delta U_{iy} =$   
 167  $\delta U_{ey} = 0.02V_0 \exp[-0.5(y/L_0)^2] \sin(2\pi x/L_x)$ . In addition, to investigate the effects of the in-  
 168 plane magnetic field, we will also show a local 2-D run (Run-D) with the same setting as Run-C  
 169 except that the in-plane field is initially set to be zero. Note that for the 3-D run (Run-B), which  
 170 used  $\sim 2 \times 10^4$  cores of MareNostrum at Barcelona Supercomputing Center (BSC) for more than  
 171  $10^2$  hours, we set up the largest system size within the computer resource limitation to reproduce  
 172 the MHD-scale ( $> d_i$ ) primary KH waves without being affected by non-MHD effects in their  
 173 initial growth phase, although the size is still about 10 times smaller than the estimated  
 174 wavelength ( $\lambda_{KH} \sim 10^{4-5}$  km  $\sim 10^{2-3}$   $d_i$ ) of the KH waves in the MMS observations (B21).

175

## 176 B. Initial equilibrium

177 In the present simulations, the pressure balance in the boundary normal ( $y$ ) direction is  
 178 satisfied in the initial conditions. However, when the magnetic field strength within the current  
 179 layer is significantly weaker than that in the outside regions like the Harris-type current sheet as  
 180 employed in the present simulations, the fluid-type equilibrium across the layer is easily  
 181 disturbed by kinetic effects. One of the main causes for this disturbance is the gyro-motion of  
 182 ions located near the center of the layer. The orbits of these ions are larger due to the smaller  
 183 magnetic field within the layer. As the simulation proceeds, the simulated particles start their  
 184 gyro-motions and the orbits of the ions that initially located near the center but on one side of the

185 layer can enter the other side of the layer because of the finite gyro-radius. When there is initially  
186 a large density jump across the layer as in the present simulations, the net number of the crossing  
187 ions that originally located on the two sides is not balanced, leading to the disturbance of the  
188 equilibrium. Fig. 1 shows the time evolutions of the 1-D profiles in the  $y$  direction of the ion  
189 density, the out-of-plane magnetic field component, and the shearing flow component for the  
190 large-scale 2-D run (Run-A). As the simulation proceeds, the high-density plasma penetrates into  
191 the lower-density side as predicted. After a few ion gyro-periods, a new quasi-equilibrium state,  
192 in which the profiles are no longer largely changed, is accomplished. Note that the KH instability  
193 starts to grow after this new equilibrium is accomplished, as will be shown in Fig. 2 and the  
194 following section.

195

### 196 III. LARGE-SCALE EVOLUTION OF KH WAVES

#### 197 A. Overview of the simulation results

198 Figs. 2a-2d show the time evolution of the ion density for Run-A. At  $t=50\Omega_i^{-1}$ , we see  
199 that 6 KH waves are growing near the center of the boundary layer (Fig. 2a). After that, a part of  
200 the surface waves, which convects towards the low-density side, grows as high-density arms  
201 penetrating into the low-density side (Figs. 2c-2d). Notice that although the arms start to roll-up  
202 a small amount, they mainly continue to grow more straight into the low-density side beyond the  
203 vortex layer and greatly disturb the layer structure. Notice also that the width of the high-density  
204 arms tends to become smaller over time as they grow in the boundary normal direction. Fig. 2e  
205 shows the growth of the 1-D power spectra ( $k_x$ ) of each  $U_{iy}$  modes. We show that in the early  
206 phase until  $t\sim 50-60\Omega_i^{-1}$ , the  $m_x=6$  mode clearly dominates, but after that the relative power of the  
207 other modes relatively gets larger corresponding to the evolution of the high-density arms, and it  
208 becomes more difficult to identify one dominant mode. As will be described in detail in Sec. IV-  
209 A, this additional evolution of the high-density arms is caused by the Rayleigh-Taylor instability  
210 (RTI) driven by the centrifugal force at the rippled surface.

211 In addition, as the large-scale surface waves develop, smaller-scale fluctuations grow,  
212 especially near the edges of the waves where the density gradient is enhanced (see, for example,  
213 a white arrow in Fig. 2a). These fluctuations are seen mainly on the low-density side of the  
214 gradient layer and penetrate deep into the lower-density region. As a result of the fluctuations,  
215 the gradient layer, where plasmas between the two sides across the layer are mixed, is

216 substantially broadened near the edges of the RTI arms. As will be described in detail in Sec. IV-  
217 B, these fluctuations result from the lower-hybrid drift instability (LHDI) driven by the thin  
218 density gradient layer formed at the edge of the primary surface waves/vortices.

219

### 220 **B. Comparison with the MMS observations**

221 To confirm the realism of the simulation, we compare the simulation results with the  
222 MMS observations of the large-scale evolution of the KH waves. Figs. 3a-3h show the virtual  
223 observations along the orbits-1 and 2 marked in Fig. 2b, while Figs. 3i-3l show the MMS  
224 observations during 15:30-16:30 UT on September 23, 2017. In the virtual observations, we  
225 assume that the spacecraft crossed the vortex layer in the direction opposite to the propagation  
226 direction of the KH waves (i.e., -x direction) at a fixed time around the transition between the  
227 linear and non-linear growth phase of the KHI ( $t=60\Omega_i^{-1}$ ). Orbit-1 crossed near the  
228 magnetosheath side edge of the bulges of the primary KH waves and vortices, while the orbit-2  
229 crossed near the center part of the waves and vortices. For orbit-2 (Figs. 3e-3h), we clearly see  
230 regular patterns of the KH waves in which the density enhancement aligns with the positive to  
231 negative  $B_L (=B_z)$  oscillation, and the minimum  $U_N$  and maximum  $P_t$  are seen near the start point  
232 of these density and  $B_L$  variations (see the variations near the vertical line in Figs. 3e-3h). For the  
233 orbit-1, these variations of the KH waves cannot clearly be seen, especially for the pressure (Fig.  
234 3d), and instead a clear density drop aligns with positive  $B_L$  and  $U_N$  peaks (see the variations  
235 near the vertical line in Figs. 3a-3d).

236 Interestingly, variations similar to the virtual observations of both orbits-1 and 2 are seen  
237 in the MMS observations shown in Figs. 3i-3l. During this one-hour interval, MMS repeatedly  
238 encountered positive-negative variations of  $B_z$  accompanied by density variations, indicating  
239 multiple encounters of the magnetopause surface waves or the oscillations of the magnetopause  
240 in the boundary normal directions. The observed variation patterns of the boundary normal  
241 vectors at these density changes strongly suggest that these variations were most likely caused by  
242 the surface waves (see Fig. 3 in B21). During the early part of this interval, MMS observed the  
243 high-density plasmas for a longer time, while at a later time, MMS observed the low-density  
244 plasmas for a longer time and more frequently encountered wave-like repeated variations,  
245 indicating that the spacecraft moved from the magnetosheath side toward the center of the layer  
246 where the surface waves were active. The variation patterns of the density,  $B_N$ ,  $V_N$  and  $P_t$  during

247 the early and later intervals are quantitatively consistent with the virtual observations for the  
248 orbit-1 and orbit-2 in the normalized units of the simulation ( $B_0=12\text{nT}$ ,  $n_0=8\text{cm}^3$ ), respectively  
249 (compare the variations near the blue vertical line in Figs. 3a-3d and the green vertical line in  
250 Figs. 3e-3h and those near the blue and green vertical lines in Figs. 3i-3l, respectively).  
251 Furthermore, given the averaged  $V_N$  during 15:40-16:00 UT (the transition between the early and  
252 later intervals)  $\langle V_N \rangle \sim +9.5$  km/s, and assuming that the magnetopause moved towards the  
253 magnetosheath side in the boundary normal direction at this speed, it is inferred that the  
254 spacecraft relatively moved about  $10^4$  km towards the magnetospheric side during 15:40-16:00  
255 UT. Since the estimated wavelength of the observed surface waves is about  $5 \times 10^4$  km, this  
256 distance corresponds to  $\sim 1/5\lambda_{KH}$ , which is roughly consistent with the distance between the  
257 orbits-1 and 2 in the boundary normal direction ( $3d_i \sim 1/5\lambda_{KH}$ ). We have confirmed that similar  
258 consistencies between the simulation and observations are seen in a range  $t \sim 60-65\Omega_i^{-1}$  (i.e., near  
259 the later linear or early non-linear growth phase of the KHI). All of these consistencies indicate  
260 that the KH waves near the later linear or early non-linear growth phase as seen in the present  
261 simulation at  $t=60\Omega_i^{-1}$  likely occur at the dusk-flank magnetopause during this interval. Note that  
262 we see the low-density and negative  $B_L$  values more frequently and for a longer time after the  
263 crossing of the green vertical line in Figs. 3i-3l, indicating that the spacecraft moved deeper into  
264 the magnetosphere. See B21 for more details of the comparisons between the present simulation  
265 and MMS observations.

266

#### 267 IV. SECONDARY INSTABILITIES

##### 268 A. Secondary RTI

269 To investigate the evolution process of the KHI and the subsequent secondary processes  
270 in more detail, we performed local 2-D and 3-D runs featuring one wavelength KH mode with a  
271 similar wavelength ( $15d_i$ ) to the fastest growing mode seen in Run-A (listed as Runs-B and C in  
272 TABLE I, respectively). In these runs, the in-plane field is initially set to be uniform. Figs. 4a-4d  
273 show the time evolution of the ion density contours for the 2-D run (Run-C). As also seen in Fig.  
274 2, for Run-A, the high-density arm penetrates deep into the low-density side, and the arm  
275 becomes narrower as the head of the arm propagates in the  $y$  direction. The growth rate of the  
276 arm, which is roughly reflected by  $m_x=2$  or 3 at least at the beginning of the arm growth as will  
277 be shown in Fig. 5 and the next paragraph, is larger than the growth rate of the primary KHI with

278  $m_x=1$  (compare the slopes of the curves in Fig. 4e). After the rapid growth of the arm (see  $t>5\alpha^{-1}$   
 279 in Fig. 4e), the amplitude of the parent KH mode ( $m_x=1$ ) is substantially reduced down to the  
 280 level comparable to the  $m_x=2+3$  modes (the sum of the amplitudes of  $m_x=2$  and 3 modes).

281 Figs. 5a-5e feature the evolution of the high-density arm during  $t=3.2\alpha^{-1}$  to  $5.6\alpha^{-1}$ , where  
 282  $\alpha^{-1}=\lambda_{KH}/V_0$  is the time unit for the growth phase of the KHI (Nakamura et al., 2013). As  
 283 mentioned above, the width of the arm becomes smaller as the arm grows in the boundary  
 284 normal direction. As highlighted by the yellow curves in Figs. 5a and 5b, this corresponds to the  
 285 decrease in the curvature radius of the head of the high-density arm. The ratio of the radius  
 286 between  $t=3.2\alpha^{-1}$  and  $3.8\alpha^{-1}$  is about  $1.7^{-1}$ , and this number is consistent with the inverse of the  
 287 square of the ratio of the growth rate of the  $m_x=2+3$  mode between  $t=3.2\alpha^{-1}$  to  $3.8\alpha^{-1}$  (see Fig.  
 288 5f). Here the  $m_x=2+3$  mode roughly corresponds to the width of the arm in the  $x$  direction (i.e.,  
 289 the width of the arm is roughly 0.3-0.5 times the wavelength of the primary KH mode) during  
 290 this time interval. Within this curved boundary layer, the current, which is produced by the anti-  
 291 parallel south-to-north magnetic field across the layer and is mainly carried by ions, flows in the  
 292 direction along the layer (see arrows in Figs. 5a-5e). Given that the strength of the current near  
 293 the density surface stays almost the same between  $t=3.2\alpha^{-1}$  to  $3.8\alpha^{-1}$ , the relation between the  
 294 curvature radius and growth rate of the head is consistent with the expected growth rate of the  
 295 RTI excited by the centrifugal force from the curved flow (Chandrasekhar, 1961; Nakamura &  
 296 Daughton, 2014);  $\gamma_{RT} \propto (U_r^2/r)^{0.5}$ , where  $U_r$  is the rotating flow speed and  $r$  is the curvature  
 297 radius of the flow. After the saturation of the  $m_x=2+3$  mode, the mushroom-like structure forms  
 298 near the head of the arm (see white arrows in Figs. 5e as well as 4c), supporting that the RTI is  
 299 secondarily induced at the density surface bent by the primary KHI, and forms the high-density  
 300 arm penetrating into the low-density side. It should be emphasized here that since the current  
 301 flows in the direction largely tilted from the KHI plane ( $\sim$  the equatorial plane) for the northward  
 302 IMF case, this RTI physics would be unique for the southward IMF case in which the current  
 303 flows nearly along the background shear flow.

304

### 305 B. 3-D effects

306 Figs. 6a-6f show the time evolution of the ion density and the  $x$ -component of the electric  
 307 field in the electron frame  $\mathbf{E}_x'=(\mathbf{E} + \mathbf{U}_e \times \mathbf{B})_x$  for the local 3-D run (Run-B) in the  $x$ - $y$  plane at

308  $z=0$ . Similar to the 2-D case in the x-y plane (see Fig. 4), the high-density arm penetrates into the  
 309 low-density side, and the size of the arm head decreases as the head moves deeper into the low-  
 310 density side. However, as shown in Fig. 6g, in the 3-D case, the high-density arm grows in the  
 311 direction somewhat tilted from the x-y plane (vortex plane), forming a large-scale wavy structure  
 312 of the arm head in the z-direction (i.e., finite  $k_z$  is produced). This tilt angle corresponds to the  
 313 direction perpendicular to the magnetic field measured at the arm head, as shown in Fig. 6h.  
 314 These features are consistent with the 3-D evolution of the RTI in the direction satisfying  $\mathbf{k} \cdot$   
 315  $\mathbf{B} \sim 0$  in which the growth rate of the RTI is maximized (Chandrasekhar, 1961). Note that in Fig.  
 316 6h we also see a weak enhancement of the wave power at around  $k_x \sim 10-20$ , which reflects the  
 317 small-scale fluctuations generated by the LHDI as will be explained in the next paragraph.

318 In the 3-D case, it is also notable that small-scale fluctuations of the electric field, which  
 319 are dominantly seen in the perpendicular components, grow mainly on the low-density side of  
 320 the density gradient layer, as seen in Figs. 6d-6f. These small-scale electric field fluctuations  
 321 produce corresponding density fluctuations and broaden the low-density side of the layer  
 322 (compare Figs. 6a-6c and 6d-6f). The amplitude of the fluctuations is locally enhanced in the thin  
 323 gradient layer compressed by the non-linearly developed primary surface wave and vortex (see  
 324 the right-side of the edge layer of the primary wave/arm in Figs. 6d-6f). The 3-D view of the  
 325 density surface in Fig. 6g shows that the wavy patterns of the small-scale density fluctuations are  
 326 nearly aligned with the local magnetic field lines, indicating that the wavevector of the  
 327 fluctuations develops in the direction nearly perpendicular to the local magnetic field. This point  
 328 is clearly seen in the power spectrum at  $t=4\alpha^{-1}$  (Figs. 7a). The power of the electric field  
 329 fluctuations is enhanced dominantly in the direction nearly perpendicular to the mean magnetic  
 330 field near the low-density side of the density gradient layer ( $k_z/k_x \sim \tan(\theta_{\text{perp}})$ ), which roughly  
 331 corresponds to the direction perpendicular to the local magnetic field in the region where the  
 332 fluctuations are enhanced. As seen in the red curve in Fig. 7c, the most strongly growing mode of  
 333 the small-scale fluctuations at  $t=4\alpha^{-1}$  is  $m_x \sim 18-23$  corresponding to the wavelength  $\sim 6.5-8 d_e$  in  
 334 the x direction. Fig. 7d shows the zoomed-in-view in the x-y plane of  $E_x'$  in the region marked in  
 335 Fig. 6d, where the fluctuations occur most strongly. The positive-negative pattern of the  
 336 fluctuations whose projected wavelength in the x direction is around  $7d_e$  is seen as expected from  
 337 the power spectrum. The tilt angle of the edge layer in the x-y plane is about  $\theta_{\text{edge}} \sim 35^\circ$ , indicating  
 338 that the actual wavelength of the dominant mode is around  $\lambda \sim 8.0-9.5 d_e$ , which is in a range of

339 the hybrid-kinetic scale based on the local ion and electron temperatures and the magnetic field  
 340 strength ( $k_{\perp}(\rho_i\rho_e)^{1/2}\sim 1.4 - 1.7$ ). The power spectrum (Fig. 7c) also shows that the enhanced  
 341 power of the fluctuations spreads nearly up to the electron kinetic scale ( $k_{\perp}\rho_e\sim 1$  corresponding  
 342 to  $m_x\sim 50-55$ ). These features (the perpendicular electric field fluctuations consisting of modes  
 343 from the hybrid-kinetic to electron kinetic scales) are consistent with the ones predicted from the  
 344 past linear analyses for the LHDI (Daughton, 2003). In the later time (see Fig. 7b), the in-plane  
 345 magnetic field is more strongly compressed near the edge of the vortex/high-density arm, leading  
 346 to  $\theta_{\text{perp}}$  being larger and the strong power seen more widely within the range  $k_x/k_x < \tan(\theta_{\text{perp}})_{\text{max}}$ .  
 347 Notice that as the peaks are scattered, the wavelength of the most strongly growing mode  
 348 becomes somewhat (1.5-2 times) longer (see the blue curve in Fig. 7c).

349 To understand the onset condition of these small-scale modes more quantitatively, a  
 350 linear dispersion relation solver for fully kinetic plasma with a perpendicular drift, which has  
 351 recently been developed in Umeda & Nakamura (2018), is applied by inputting parameters  
 352 obtained from the simulation. In this solver, the dispersion relation is derived in the  
 353 electromagnetic and fully kinetic regime for ions and electrons that drift in the direction  
 354 perpendicular to the magnetic field, which can include ion and electron cyclotron resonances  
 355 unlike the conventional approximation by Davidson et al. (1977) (see Umeda & Nakamura  
 356 (2018) for more details about this linear dispersion relation). This solver requires  $m_i/m_e$  and local  
 357 values of the ion-to-electron temperature ratio  $T_i/T_e$ ,  $\omega_{pe}/\omega_{ce}$ , the ion and electron drift velocities  
 358 relative to the thermal speeds  $V_d/V_i$ , and the ratio between the thermal speeds and the speed of  
 359 light  $V/c$  for ions and electrons as input parameters to obtain the dispersion relation. Fig. 7f  
 360 shows the results of the linear analysis in which the input parameters are obtained as local values  
 361 at the location marked in Fig. 4b. Note that the parameters are obtained at the location where the  
 362 small-scale fluctuations are most strongly seen in the 3-D run (Run-B) but from the  
 363 corresponding 2-D run (Run-C) in which the fluctuations are suppressed and thus we can obtain  
 364 stable background values. The obtained parameters are  $m_i/m_e=100$ ,  $T_i/T_e=3.7$ ,  $\omega_{pe}/\omega_{ce}=1.8$ ,  
 365  $V_{di}/V_{ti}=0$ ,  $V_{de}/V_{te}=0.16$ ,  $V_{ii}/c=0.05$ , and  $V_{ie}/c=0.26$  ( $\beta\sim 2.1$ ). The dispersion relation demonstrates  
 366 that a quasi-perpendicular wave mode with a wave normal angle of  $\phi\sim 87^\circ$  relative to the ambient  
 367 magnetic field has the maximum growth rate  $\gamma\sim 0.06\omega_{LHR}$  at a wave number  $m_{LH} =$   
 368  $k_{\perp}(\rho_i\rho_e)^{1/2}\sim 1.6$ , where  $\omega_{LHR}$  is the lower-hybrid frequency. Considering the tilt angle of the  
 369 gradient layer in the x-y plane  $\theta_{\text{edge}}\sim 35^\circ$  as discussed above, the dominant mode seen in the



370 simulation is in excellent agreement with the fastest growing mode obtained from the linear  
 371 analysis as seen in the red curve in Fig. 7c. This clearly indicates that the  $E_{\perp}$  fluctuations seen in  
 372 the simulation are caused by the perpendicular plasma drifts and the related growth of the LHDI.

373 Notice that the dispersion relation for a mode with  $\phi \sim 89^{\circ}$  in Fig. 7f shows a significantly  
 374 low frequency below the ion cyclotron frequency ( $< 0.1\omega_{LHR}$ ), which indicates that some modes  
 375 could be largely affected by the ion gyro-motion in the present simulation. This could be because  
 376 when the ion-to-electron mass ratio is low, as in the present simulation ( $m_i/m_e=100$ ), the gyro-  
 377 radius of a large portion of ions can be comparable to or smaller than the wavelength of the  
 378 electric field fluctuations (i.e., hybrid-kinetic scale), and hence their motions can largely affect  
 379 the evolution of the waves in addition to electron motions. For example, in the present case, the  
 380 ratio between the ion gyro-radius and the wavelength of the fluctuations  $\alpha_{IC} = \rho_i / [2\pi(\rho_i\rho_e)^{1/2} /$   
 381  $m_{LH}] = (m_{LH}/2\pi) \cdot (m_i/m_e)^{1/4} \cdot (T_i/T_e)^{1/4} \sim 0.7m_{LH}$ . This number becomes larger as the mass  
 382 ratio increases, and would greatly exceed one (i.e., the ion kinetic effects would be negligible) in  
 383 a realistic ( $m_i/m_e=1836$ ) case. Indeed, the linear analyses for larger mass ratio cases with  
 384  $m_i/m_e=256$  (Fig. 7g) and  $m_i/m_e=1836$  (Fig. 7h) show that the most unstable modes would be in a  
 385 range of the pure LHDI without being significantly affected by the ion gyro-motion (i.e.,  $\alpha_{IC} \gg$   
 386 1). Here the input parameters to the linear dispersion relation solver for these high  $m_i/m_e$  cases  
 387 are set to be the same as the case for Fig. 7f except for higher  $m_i/m_e$  and corresponding larger  
 388  $\omega_{pe}/\omega_{ce}$  and  $V_{te}/c$ . An additional simulation for  $m_i/m_e=256$ , in which the initial settings are the  
 389 same as Run-B except for smaller  $L_y (=2d_i)$  and 1.6 ( $= (256/100)^{0.5}$ ) times smaller grid-spacing,  
 390 shows that the dominant mode for  $m_i/m_e=256$  is indeed  $m_{LH} \sim 3$  (Fig. 7e) as predicted from the  
 391 linear analysis (Fig. 7g), supporting the predictions from the linear analyses.

392 Based on the above consistencies between the simulation and the linear analysis, we  
 393 further applied the linear dispersion relation solver to real parameters obtained from the MMS  
 394 observation event treated in this paper and B21. The input parameters, based on local values near  
 395 the time interval with large amplitudes of the field fluctuations at the trailing edge of the KH  
 396 waves, shown in Fig. 10 in B21 ( $\sim 15:56$  UT), are  $m_i/m_e=1836$ ,  $T_i/T_e=11.6$ ,  $\omega_{pe}/\omega_{ce}=21.4$ ,  
 397  $V_{di}/V_{ti}=0$ ,  $V_{de}/V_{te}=0.12$ ,  $V_{ti}/c=0.0012$ , and  $V_{te}/c=0.015$  ( $\beta \sim 2.5$ ). Fig. 7i shows the results of the  
 398 linear analysis for this MMS event. Similar to the above simulation cases, a quasi-perpendicular  
 399 wave mode with  $\phi \sim 87^{\circ}$  relative to the ambient magnetic field has the maximum growth rate  
 400  $\gamma \sim 0.2\omega_{LHR}$  at a wave number  $k_{\perp}(\rho_i\rho_e)^{1/2} \sim 3$ . This wave number corresponds to  $\lambda \sim 56$  km. Given

401 the simulation result that the wavelength of the dominant modes tends to become 1.5-2 times  
402 longer as the LHDI develops (see blue curve in Fig. 7c), this predicted wavelength of the fastest  
403 growing mode is in reasonable agreement with the estimation from the observed field  
404 fluctuations in this MMS event (~80-100 km) (see B21 for more details of the MMS  
405 observations of the small-scale field fluctuations between the KH waves). Together with the  
406 above quantitative consistencies between the simulation and the MMS event on the large-scale  
407 evolution of the primary KHI/RTI shown in Sec III-B, these results naturally suggest that the  
408 LHDI-driven turbulence at the edges of the KHI/RTI waves/vortices as seen in the present  
409 simulation may occur in the Earth's magnetopause during the southward IMF.

410

### 411 C. Turbulent reconnection

412 The top panels in Fig. 8 show the  $B_z$  component in the  $x$ - $y$  plane at  $t=5.4\alpha^{-1}$  (early non-  
413 linear growth phase of the KHI) in the 3-D case (Run-B), the corresponding 2-D case (Run-C),  
414 and the 2-D case without the initial in-plane magnetic field (Run-D). The initial anti-parallel  
415 magnetic field forms the thin primary current layer (corresponding to the density gradient layer)  
416 along the edge of the large-scale surface wave in all cases. However, the small-scale fluctuations  
417 induced by the LHDI disturb and broaden the upper positive- $B_z$  side (low-density side) of the  
418 layer for Runs-B and D. Note that for Run-C, the in-plane magnetic field, which is locally  
419 compressed and enhanced along the edge of the surface wave (see black curves in Fig. 8d),  
420 prevents the small-scale fluctuations from growing (i.e., the quasi-perpendicular unstable LHDI  
421 modes do not exist in the 2-D simulation plane), while for Run-B, a similar enhancement of the  
422 in-plane field is seen but the LHDI can grow obliquely in the direction nearly perpendicular to  
423 the magnetic field as shown in the above section. The middle panels in Fig. 8 show the  $J_z$   
424 component for the three runs, while the bottom panels show the time evolution of the global  
425 reconnection rate computed from the integrated magnetic flux that crosses the (mixing) surfaces  
426 of the layer on the low-density and positive- $B_z$  (top) and the high-density and negative- $B_z$   
427 (bottom) sides (Daughton et al., 2014). For Runs-B and C, the compressed in-plane field  
428 produces strong out-of-plane currents ( $J_z$ ) mainly in the low-density side of the primary gradient  
429 layer (Figs. 8b and 8e). For Run-B, the magnetic flux rapidly flows into the low-density side of  
430 the primary layer (Fig. 8c). These results indicate that magnetic reconnection occurs within the  
431 low-density side of the layer where the strong  $J_z$  (i.e., the large magnetic shear) is produced by

432 the compressed in-plane field as mentioned above. Note that since the surfaces of the z-  
433 component of the vector potential do not exactly correspond to the in-plane field lines in 3-D, the  
434  $J_z$  variations for Run-B (Fig. 8b) are not exactly aligned with the surfaces of the potential (black  
435 curves in Fig. 8b), especially near the head of the high-density arm where the magnetic field  
436 lines are three-dimensionally twisted (Fig. 6g). Note also that we see no significant enhancement  
437 of the inflowing flux in the 2-D cases (Figs. 8f and 8i). This is because the unstable mode of the  
438 tearing instability satisfying  $\mathbf{k} \cdot \mathbf{B} = 0$  cannot be found in the 2-D simulation planes (i.e., there  
439 is no anti-parallel, in-plane component of the magnetic field).

440 It is notable that the rate of the flux inflow on the high-density side for Run-B (see the red  
441 curve in Fig. 8c) is about 10 times smaller than that on the low-density side ( $R \sim 0.5$ ). This  
442 indicates that in this 3-D case, reconnection occurs mostly on the low-density side and hardly  
443 occurs between the two sides across the primary layer (i.e., between the northward and  
444 southward magnetic field lines across the magnetopause). This could be because the small-scale  
445 fluctuations broaden the low-density side of the layer and prevent the inflowing flux on the low-  
446 density side from reaching the high-density side across the layer. This result is not seen in recent  
447 3-D fully kinetic simulations in the southward IMF case (Nakamura et al., 2020a), in which the  
448 initial density jump is set to be weak ( $n_{10}/n_{20}=3.0$ ), no significant evolution of the LHDI  
449 fluctuations is seen, and reconnection strongly develops across the layer. Note that a weak  
450 enhancement of the flux inflow rate on the high-density side is seen not only for Run-B but also  
451 for Run-D in which reconnection cannot occur in the 2-D simulation plane (see the red curves in  
452 Figs. 8c and 8i). These weak enhancements on the high-density side result from the mixing  
453 caused by the LHDI fluctuations.

454

#### 455 **D. Plasma transport and mixing**

456 Fig. 9a shows the time evolution of the thickness in the boundary normal (y) direction of  
457 the region where the profile in the x-direction contains the density variation larger than  $0.3(n_{10}-$   
458  $n_{20})$ , for Runs B-D. This thickness roughly corresponding to the penetration distance of the high-  
459 density arm into the low-density side. For all runs, we see a similar continuous penetration of the  
460 arm, corresponding to a similar evolution of the large-scale KHI/RTI (see also top panels in Fig.  
461 8), at a speed  $0.3-0.4V_0$  until  $t \sim 6\alpha^{-1}$ . Note that for Runs B-D, the penetration is suppressed at  
462  $t \sim 6\alpha^{-1}$  by the effects of the simulation boundaries in the y-direction, while for Run-A, in which

463 the system size is set to be larger than that for Runs B-D, the penetration continues even after  
 464  $t \sim 6\alpha^{-1}$  without being affected by the boundaries (see the black curve in Fig. 9a).

465 Fig. 9b shows the time evolution of the averaged thickness in the y direction of the  
 466 mixing region defined as the region with  $|F_e| < 0.99$  for Runs B-D. We clearly see that for Runs-B  
 467 and D, in which the LHDI turbulence occurs, the mixing region expands much more efficiently  
 468 than Run-C. This indicates that the LHDI turbulence dominantly contributes to the mixing  
 469 between the high- and low-density sides in the vortex layer, while the RTI and the resulting  
 470 penetration of the high-density arm, which contribute to the convective transport of high-density  
 471 plasmas into the low-density side as shown in Fig. 9a, do not significantly contribute to the  
 472 plasma mixing between the two sides.

473

#### 474 **E. Detection probability of the primary KH mode**

475 Similar evolutions of the high-density arm for all runs shown in Fig. 9a indicate that the  
 476 local mixing by the LHDI turbulence does not significantly disturb the large-scale evolution of  
 477 the KHI and RTI – i.e., the primary KHI and the subsequent secondary RTI are the dominant  
 478 processes to control the large-scale evolution of the shear layer. As described in Sec. IV-A,  
 479 during this large-scale evolution of the layer, the high-density arm becomes narrower as the arm  
 480 develops in the boundary normal direction. This suggests that when the spacecraft crosses the  
 481 vortex layer, the observed dominant mode would be different at different locations (relative to  
 482 the high-density arm) and/or at different times (depending on the growth phases of the KHI and  
 483 RTI). Figs. 10a and 10b show  $k_x$  spectra for Run-B of the total pressure for each y  
 484 (corresponding to the spectra from the virtual observations in which the virtual probe crosses the  
 485 layer in the x direction at each y) at  $t=3\alpha^{-1}$  and  $t=6\alpha^{-1}$  (before and after the onset of the RTI). At  
 486  $t=3\alpha^{-1}$ , a dominant mode of the KHI ( $m_x=1$ ) is clearly seen near  $y=0$ , while at  $t=6\alpha^{-1}$ , smaller-  
 487 scale modes become visibly stronger especially at the low-density side ( $y>0$ ) and it is no longer  
 488 easy to identify one dominant mode. Notice that this flattening of the spectra corresponds to the  
 489 formation of intermittent and irregular variation patterns of the surface waves as shown in Figs.  
 490 3a-3h for Run-A.

491 Figs. 10c and 10d show the  $k_x$  spectra integrated over y of the total pressure and the y  
 492 component of the ion bulk velocity. At  $t=3\alpha^{-1}$ , the amplitude of the primary KH ( $m_x=1$ ) mode is  
 493 more than one order of magnitude larger than that of the smaller-scale modes, while at  $t=6\alpha^{-1}$

494 and later times, the difference in the amplitude between the KHI and smaller-scale modes  
495 becomes much smaller. Fig 10f shows the time evolution of the ratio of the amplitude of the  
496 primary KH ( $m_x=1$ ) mode and the smaller-scale ( $m_x=2-8$ ) modes. The ratio becomes below 10  
497 (i.e., the amplitudes of the primary KH and smaller scale modes become within an order of  
498 magnitude) at  $t\sim 3.5-4\alpha^{-1}$ , indicating that it quickly becomes difficult to identify the primary KH  
499 mode just after the onset of the secondary RTI ( $t\sim 3\alpha^{-1}$ ). As shown in Fig. 10e (the same as the  
500 red curve in Fig. 9a), the decrease of the ratio roughly corresponds to the evolution of the high-  
501 density arm. These results may explain the low observational probability of the KH waves during  
502 southward IMF periods (e.g., Kavosi & Raeder, 2015) - i.e., during southward IMF, even when  
503 the KHI is unstable at the magnetopause, the evolution of the secondary RTI and the resulting  
504 penetration of the high-density arm could make it difficult to identify the periodic KH waves.  
505

## 506 V. SUMMARY AND DISCUSSION

### 507 A. Summary

508 Based on 2-D and 3-D fully kinetic simulations of the MMS event on September 23,  
509 2017, in which signatures of the KH waves were observed during a southward IMF interval as  
510 shown in our companion paper B21, we investigated the evolution process of the KH waves and  
511 related secondary waves/instabilities during the southward IMF. The main results of this paper  
512 are summarized as follows:

- 513 1. The KHI is indeed unstable and forms surface waves at the magnetopause boundary layer  
514 (velocity shear layer) under the parameters obtained from the MMS observations during  
515 southward IMF on September 23, 2017.
- 516 2. As the primary KHI grows, the ion current, which is produced by the anti-parallel (south-  
517 north) magnetic field across the surface and flows in the direction nearly parallel to the  
518 background shear flow (i.e., in the equatorial plane), is bent in the boundary normal direction  
519 and drives the secondary RTI.
- 520 3. The growth of the RTI results in the penetration of high-density arms into the low-density  
521 (magnetospheric) side, which disturbs the vortex motion and significantly reduces the  
522 observational probability of the primary KH waves.

- 523 4. At the edge of the KH waves and the high-density arms, where the thin density gradient layer  
 524 forms, the LHDI is induced and produces the small-scale (hybrid kinetic-scale) fluctuations  
 525 in the perpendicular component of the electric field. The LHDI grows mainly in the low-  
 526 density side of the gradient layer, leading to the diffusion of the layer.
- 527 5. The secondary RTI and the resulting penetration of the high-density arms cause plasma  
 528 transport into the low-density side, while the LHDI contributes to the plasma mixing along  
 529 the edge of the primary KH waves and the high-density arms.
- 530 6. Although signatures of magnetic reconnection (inflowing magnetic flux) are observed within  
 531 the LHDI turbulence, reconnection does not significantly grow across the primary shear  
 532 layer.
- 533 7. The large-scale variations of the surface waves by the KHI and RTI and the small-scale  
 534 fluctuations by the LHDI are reasonably consistent with those seen in the MMS observations  
 535 (see B21 for details of the MMS observations).

536

537 **B. IMF dependence**

538 A key difference in the profile across the low-latitude magnetopause between the  
 539 northward and southward IMF cases is the direction (and the amplitude) of the current produced  
 540 by the magnetic shear between the magnetosheath and magnetospheric sides compared to the  
 541 background shear flow (the equatorial plane). During the northward IMF, the magnetopause  
 542 current is weaker and flows in the direction largely tilted from the shear flow, while during  
 543 southward IMF, stronger current flows in the direction closer to the shear flow. As shown in Sec.  
 544 IV-A, during southward IMF, this strong in-plane current causes the secondary RTI at the  
 545 boundary layer bent by the KH waves, leading to the deep penetration of the high-density arm  
 546 into the magnetospheric side. Here, the ratio of the growth rates of the primary KHI and the  
 547 secondary RTI can roughly be estimated in the incompressible MHD regime (Chandrasekhar,  
 548 1961) as

$$549 \quad \frac{\gamma_{KH}}{\gamma_{RT}} \sim \sqrt{\frac{(k_{KH}V_0)^2}{k_{RT}(V_{MP}^2/r)}} = \sqrt{\frac{r\lambda_{RT}}{\lambda_{KH}^2}} \frac{V_0}{V_{MP}},$$

550 where  $k_{KH}$ ,  $k_{RT}$ ,  $\lambda_{KH}$  and  $\lambda_{RT}$  are the wavenumber and wavelength of the KHI and RTI,  
551 respectively,  $r$  is the curvature radius of the surface wave, and  $V_{MP}$  is the parallel (to the shear  
552 flow) velocity component of ions that partly carry the magnetopause current. Assuming that the  
553 current is carried only by ions with typical parameters near the flank magnetopause as the layer  
554 thickness  $L_{MP} \sim 10^3$  km, the magnetic field varying from -20 nT to 20 nT across the layer (i.e.,  
555  $\Delta B_z \sim 40$  nT) and the density near the center of the layer  $n_{MP} \sim 1 \text{ cm}^{-3}$ ,  $V_{MP}$  is roughly estimated as  
556  $V_{MP} \sim (\Delta B_z / L_{MP}) / (\mu_0 e n_{MP}) \sim 200$  km/s, which is comparable to the amplitude of the shear flow  
557 near the flank magnetopause (i.e.,  $V_{MP} \sim V_0$ ). Since  $\lambda_{RT}$  and  $r$ , both of which depend on  $\lambda_{KH}$ , are  
558 only a few times smaller than  $\lambda_{KH}$  and comparable to  $\lambda_{KH}$ , respectively, as shown in Sec. IV-A,  
559 the growth rate of the secondary RTI would commonly be comparable to that of the primary KHI  
560 at the flank magnetopause. Thus, the strong growth of the RTI and the resulting deep penetration  
561 of the high-density arm as seen in the present simulations could actually occur at the flank  
562 magnetopause during southward IMF.

563 The black dashed curves in Figs. 10e and 10f show the results from the 3D run of an  
564 MMS observation event of KH waves during northward IMF on September 8, 2015 (Nakamura  
565 et al., 2017a,b, Nakamura, 2021). In this northward IMF case, the vortex-induced reconnection  
566 quickly destroys the structure of the primary KH vortex (Nakamura et al., 2017b), leading to the  
567 quick decrease of the relative amplitude of the primary KH mode as seen in Fig. 10f.  
568 Interestingly, the decrease rate in the present simulation for southward IMF is somewhat larger  
569 than the simulation for northward IMF (compare red solid and black dashed curves in Fig. 10f).  
570 This could be because of the quicker evolution of the high-density arm due to the RTI for the  
571 southward IMF case (compare red solid and black dashed curves in Fig. 10e). This result  
572 indicates that it would be rather difficult to identify the KH waves from the periodicity of the  
573 surface waves during southward IMF even when the unstable condition for the KHI is satisfied.  
574 In addition, notice that the evolution of the high-density arm for the southward IMF leads to  
575 intermittent and irregular variation patterns of the plasma and field parameters as shown in Figs.  
576 3a-3h. Similar variation patterns were observed in the MMS event treated in this paper (see Figs.  
577 3i-3l) as well as the past observation of the KH waves during southward IMF by Cluster (Hwang  
578 et al., 2011). Combined with similar estimated growth rates of the RTI and KHI, the intermittent  
579 and irregular variation patterns of the surface waves would be a common feature of KH waves  
580 observed during southward IMF.

581

582 **C. Some remarks on future work**

583 Recent 3-D kinetic simulations of the magnetopause KHI showed that reconnection  
584 induced by the magnetic shear across the magnetopause quickly decays the non-linear vortex  
585 structure for both northward (Nakamura et al., 2017a,b) and southward (Nakamura et al., 2020a)  
586 IMF cases. On the other hand, in the present simulation which has a density jump across the  
587 magnetopause that is more than two times higher than the jumps employed in these recent  
588 simulations, the secondary RTI and LHDI driven by the large density gradient are the main  
589 processes that control the non-linear vortex structure, and reconnection occurs only locally  
590 within the LHDI turbulence. These results suggest that while reconnection plays a key role in  
591 controlling the non-linear KH vortex structure for both northward and southward IMFs if the  
592 density jump across the magnetopause is sufficiently small, as the density jump becomes larger,  
593 the secondary RTI and LHDI become more active and can play a more significant role in  
594 controlling the vortex structure. We expect the density jump to be generally larger for southward  
595 IMF conditions when the LLBL is thinner or less prominent than for northward IMF (Mitchell et  
596 al., 1987). An additional survey on the density ratio across the magnetopause would lead to a  
597 more systematic understanding of the secondary reconnection, RTI and LHDI processes and  
598 their dependence on the density ratio across the magnetopause.

599 In the present 3-D simulation, as shown in Sec. IV-A, the secondary RTI dominates  
600 plasma transport into the low-density side and strongly disturbs the large-scale vortex structure,  
601 while as shown in Sec. IV-B, the secondary LHDI broadens the low-density side of the density  
602 gradient layer where plasmas are mixed across the layer. Assuming that the primary KHI, whose  
603 wavelength and phase speed are  $\lambda_{KH} \sim 10^{4-5}$  km and  $V_{ph} \sim V_0 \sim 200-300$  km/s, respectively, starts  
604 growing near the dayside-to-flank magnetopause, since the secondary processes are driven in the  
605 non-linear growth phase of the primary KHI, which corresponds to  $\Delta x \sim V_0 4\alpha^{-1} \sim 4\lambda_{KH}$ —a few to  
606 50 Earth radii from the onset location of the primary KHI, the vortex-induced diffusive plasma  
607 transport and mixing would be active at the flank-to-tail magnetopause during southward IMF.

608 However, to more quantitatively understand these diffusive processes, further simulations  
609 under more realistic conditions would be required. For example, as shown in Fig. 7, since the  
610 growth rate of the LHDI and the related ion-kinetic effects depend on the ion-to-electron mass



611 ratio, to understand the actual roles of the LHDI turbulence (as well as reconnection within the  
612 turbulence), larger-scale simulations with higher mass ratios would need to be performed. In  
613 addition, although the evolution of the secondary RTI would not be significantly affected by the  
614 mass ratio, as shown in Fig. 10a, the depth that the high-density arm can penetrate into the low-  
615 density side depends on the simulation system size. Thus, to estimate the actual transport rate  
616 and understand the role of the RTI, larger-scale simulations would also need to be performed.  
617 Furthermore, since the pure (i.e., non-KHI-related) reconnection process and related phenomena  
618 such as flux transfer events frequently occur at the low-latitude magnetopause during southward  
619 IMF (e.g., Fuselier, 2021 and references therein), to more comprehensively understand the local  
620 physics of the KHI, it would also be required to consider the global coupling with the other  
621 processes. Although it is difficult to include these global physics in the fully kinetic regime,  
622 global hybrid (fluid-electron and kinetic-ions) simulations, which recently became applicable to  
623 the whole Earth's magnetosphere (e.g., Palmroth et al., 2018; Guo et al., 2021), may provide  
624 important support for treating such global inter-process couplings.

625 As discussed above, the estimated ion velocity component produced by the magnetopause  
626 current  $V_{MP}$  ( $\sim 200$  km/s) is close to the background velocity shear across the magnetopause  
627 ( $V_{MP} \sim V_0$ ). Although  $V_{MP}$  is basically dominant within the current layer and the shearing flow  
628 component is less effective within the current layer, the shearing flow can modify the total flow  
629 profile to some degree. At the dusk-side magnetopause as in the present MMS event, the  
630 direction of the shearing flow is close to that of the ion current, and therefore the shearing flow  
631 can enhance the total flow and strengthen the growth of the RTI, while on the dawn-side, the  
632 direction of the shearing flow is mostly opposite from the ion current and therefore the RTI can  
633 be weakened. This effect would increase with increasing down tail distance, as the velocity shear  
634 becomes stronger. Thus, there may be a local-time difference in the plasma transport rate by the  
635 KHI/RTI during southward IMF. Systematically surveying the local-time dependence would also  
636 be important to more practically understand the effects of the magnetopause KHI during  
637 southward IMF.

638 Finally, it should be noted that the present simulations started from a Harris-type current  
639 layer in which the total pressure within the layer is sustained by the plasma pressure and the  
640 magnetic field strength within the layer is weaker than that in the background regions. Although  
641 no significant decrease of the magnetic field strength near the current layer crossings of this

642 MMS event (for example, see Fig. 3 in B21) may indicate that the observed KH waves were  
643 driven at a non-Harris-type layer, it is difficult to know the exact initial equilibrium conditions  
644 from the observations. Past observational and analytical studies of the Earth's magnetopause  
645 crossings showed that in addition to the Harris-type layer, the force-free configuration of the  
646 current layer, in which the magnetic field strength is nearly constant across the layer, also exists  
647 at the magnetopause (Panov et al., 2011). Investigating these different types of the initial current  
648 layers would be required to more systematically understand the evolution process of the  
649 magnetopause KH waves during southward IMF.

## 650 VI. CONCLUSIONS

651 We have performed a series of 2-D and 3-D fully kinetic simulations of an MMS  
652 observation event on September 23, 2017, in which the KH waves were observed at the dusk-  
653 flank magnetopause during southward IMF. This is the first numerical challenge to investigate  
654 the magnetopause KHI under realistic parameters for the southward IMF. The simulations  
655 demonstrate (i) that the KHI is unstable under the parameters of this MMS event, (ii) that the  
656 growth of the secondary RTI and the subsequent penetration of high-density arms into the low-  
657 density side disturb the primary vortex structure and produce intermittent and irregular variations  
658 of the surface waves, leading to a low observational probability of the primary KH waves, and  
659 (iii) that the secondary LHDI induced near the vortex edge causes the efficient plasma mixing  
660 across the magnetopause. The large-scale variations of the surface waves and the small-scale  
661 fluctuations from the LHDI are reasonably consistent with the MMS observations. These results  
662 indicate that the multi-scale secondary processes and the resulting plasma transport and mixing  
663 as shown in the present simulations may actually occur at the flank-to-tail magnetopause during  
664 southward IMF.

665

## 666 ACKNOWLEDGMENTS

667 This work was supported by the Austrian Research Fund (FWF): P32175-N27. For the  
668 simulations employed in this paper, we acknowledge PRACE for awarding us access to  
669 MareNostrum at Barcelona Supercomputing Center (BSC), Spain. A part of the simulation data  
670 was analyzed with resources at the Space Research Institute of Austrian Academy of Sciences.  
671 The observation data employed in this paper were obtained from the MMS spacecraft and are  
672 publicly available via NASA resources and the Science Data Center at CU/LASP

This is the author's peer reviewed, accepted manuscript. However, the online version of record will be different from this version once it has been copyedited and typeset.

PLEASE CITE THIS ARTICLE AS DOI: 10.1063/1.50067391

Manuscript submitted to Physics of Plasmas

673 (<https://lasp.colorado.edu/mms/sdc/public/>). The work by H.H. was supported by JSPS Grant-in-  
 674 aid for Scientific Research KAKENHI 21K03504. J.E.S was supported by the Royal Society  
 675 University Research Fellowship URF/R1\201286.  
 676

677 **DATA AVAILABILITY**

678 The simulation data shown in this paper are available online via  
 679 <http://doi.org/10.5281/zenodo.5725490>.  
 680

681 **REFERENCES**

- 682 Blasl, K. A., T. K. M. Nakamura, F. Plaschke, R. Nakamura, H. Hasegawa, J. E. Stawarz, Y. –H.  
 683 Liu, S. A. Peery, J. C. Holmes, M. Hosner, D. Schmid, O. W. Roberts, and M. Volwerk,  
 684 Multi-scale observations of the magnetopause Kelvin-Helmholtz waves during southward  
 685 IM, *Physics of Plasmas*, accepted (B21).
- 686 Bowers, K. J., B. J. Albright, L. Yin, B. Bergen, and T. J. T. Kwan, Ultrahigh performance three-  
 687 dimensional electromagnetic relativistic kinetic plasma simulation, *Phys. Plasmas* **15**,  
 688 055703 (2008).
- 689 Bowers, K. J., B. J. Albright, L. Yin, W. Daughton, V. Roytershteyn, B. Bergen and T. J. T.  
 690 Kwan, Advances in petascale kinetic simulations with VPIC and Roadrunner, *J. Phys.:  
 691 Conf. Series* **180**, 012055 (2009).
- 692 Burch, J. L., T. E. Moore, R. B. Torbert, and B. L. Giles, Magnetospheric Multiscale overview  
 693 and science objectives, *Space Sci. Rev.*, 199, 5–21 doi:10.1007/s11214-015-0164-9  
 694 (2016).
- 695 Cassak, P. A., and A. Otto, Scaling of the magnetic reconnection rate with symmetric shear flow,  
 696 *Physics of Plasmas*, 18, 074501 (2011); doi: 10.1063/1.3609771 (2011).
- 697 Chandrasekhar, S., *Hydrodynamic and Hydromagnetic Stability*, Oxford Univ. Press, New York  
 698 (1961).
- 699 Daughton, W., Electromagnetic properties of the lower-hybrid drift instability in a thin current  
 700 sheet, *Phys. Plasmas*, 10, 3103, doi:10.1063/1.1594724 (2003).

- 701 Daughton, W., T. K. M. Nakamura, H. Karimabadi, V. Roytershteyn, and B. Loring, Computing  
702 the reconnection rate in turbulent kinetic layers by using electron mixing to identify  
703 topology, *Physics of Plasmas* **21**, 052307 (2014).
- 704 Davidson, R. C., N. T. Gladd, C. S. Wu, and J. D. Huba, Effects of finite plasma beta on the  
705 lower-hybrid-drift instability, *Phys. Fluids*, **20**, 301–310, doi:10.1063/1.861867 (1977).
- 706 Guo, J., Lu, S., Lu, Q., Lin, Y., Wang, X., Huang, K., Wang, R., Wang, S., Structure and  
707 coalescence of magnetopause flux ropes and their dependence on IMF clock angle:  
708 Three-dimensional global hybrid simulations. *Journal of Geophysical Research: Space*  
709 *Physics*, **126**, e2020JA028670. <https://doi.org/10.1029/2020JA028670> (2021).
- 710 Eriksson, S., B. Lavraud, F. D. Wilder, J. E. Stawarz, B. L. Giles, J. L. Burch, W. Baumjohann,  
711 R. E. Ergun, P.-A. Lindqvist, W. Magnes, et al., Magnetospheric Multiscale observations  
712 of magnetic reconnection associated with Kelvin-Helmholtz waves, *Geophys. Res. Lett.*,  
713 **43**, 5606-5615, doi:10.1002/2016GL068783 (2016a).
- 714 Eriksson, S., F. D. Wilder, R. E. Ergun, S. J. Schwartz, P. A. Cassak, J. L. Burch, L.-J.  
715 Chen, R. B. Torbert, T. D. Phan, B. Lavraud, et al., Magnetospheric Multiscale  
716 Observations of the Electron Diffusion Region of Large Guide Field Magnetic  
717 Reconnection, *Phys. Rev. Lett.* **117**, 015001 (2016b).
- 718 Fairfield, D. H., and A. Otto, T. Mukai, S. Kokubun, R. P. Lepping, J. T. Steinberg, A. J.  
719 Lazarus, T. Yamamoto, Geotail observations of Kelvin-Helmholtz instability at the  
720 equatorial magnetotail boundary for parallel northward fields, *J. Geophys. Res.*, **105**,  
721 21,159, doi:10.1029/1999JA000316 (2000).
- 722 Fairfield, D. H., M. M. Kuznetsova, T. Mukai, T. Nagai, T. I. Gombosi, and A. J. Ridley, Waves  
723 on the dusk flank boundary layer during very northward interplanetary magnetic field  
724 conditions: Observations and simulation, *J. Geophys. Res.*, **112**, A08206,  
725 doi:10.1029/2006JA012052 (2007).
- 726 Foullon, C., C. J. Farrugia, A. N. Fazakerley, C. J. Owen, F. T. Gratton, and R. B. Torbert,  
727 Evolution of Kelvin-Helmholtz activity on the dusk flank magnetopause, *J. Geophys.*  
728 *Res.*, **113**, A11203, doi:10.1029/2008JA013175 (2008).

This is the author's peer reviewed, accepted manuscript. However, the online version of record will be different from this version once it has been copyedited and typeset.

PLEASE CITE THIS ARTICLE AS DOI: 10.1063/5.0067391

Manuscript submitted to Physics of Plasmas

- 729 Fuselier, S. A., Dayside Magnetopause Processes, *Chapter 10 in "Solar/heliosphere 2,*  
730 *Magnetospheres of the solar system"* (AGU Book), Wiley (2021).
- 731 Hasegawa, H., M. Fujimoto, T.-D. Phan, H. Rème, A. Balogh, M. W. Dunlop, C.  
732 Hashimoto and R. TanDokoro, Transport of solar wind into Earth's magnetosphere  
733 through rolled-up Kelvin-Helmholtz vortices, *Nature*, **430**, 755, doi:10.1038/nature02799  
734 (2004).
- 735 Hasegawa, H., M. Fujimoto, K. Takagi, Y. Saito, T. Mukai, and H. Rème, Single-spacecraft  
736 detection of rolled-up Kelvin-Helmholtz vortices at the flank magnetopause, *J. Geophys.*  
737 *Res.*, *111*, A09203, doi:10.1029/2006JA011728 (2006).
- 738 Hasegawa, H., T. K. M. Nakamura, D. J. Gershman, Y. Nariyuki, A. F.- Viñas, B. L. Giles, B.  
739 Lavraud, C. T. Russell, Y. V. Khotyaintsev, R. E. Ergun and Y. Saito, Generation of  
740 turbulence in Kelvin-Helmholtz vortices at the Earth's magnetopause: Magnetospheric  
741 Multiscale observations. *Journal of Geophysical Research: Space Physics*, *125*,  
742 e2019JA027595. <https://doi.org/10.1029/2019JA027595> (2020).
- 743 Hwang, K.-J., M. M. Kuznetsova, F. Sahraoui, M. L. Goldstein, E. Lee, and G. K. Parks, Kelvin-  
744 Helmholtz waves under southward interplanetary magnetic field, *J. Geophys. Res.*, *116*,  
745 A08210, doi:10.1029/2011JA016596 (2011).
- 746 Hwang, K.-J., Dokgo, K., Choi, E., Burch, J. L., Sibeck, D. G., Giles, B. L., H. Hasegawa, H. S.  
747 Fu, Y. Liu, Z. Wang, T. K. M. Nakamura et al., Magnetic reconnection inside a flux rope  
748 induced by Kelvin-Helmholtz vortices. *Journal of Geophysical Research: Space*  
749 *Physics*, *125*, e2019JA027665. <https://doi.org/10.1029/2019JA027665> (2020).
- 750 Kavosi, S. and J. Raeder, Ubiquity of Kelvin-Helmholtz waves at Earth's magnetopause. *Nat.*  
751 *Commun.* *6*:7019 doi: 10.1038/ncomms8019 (2015).
- 752 Kokubun, S., H. Kawano, M. Nakamura, T. Yamamoto, K. Tsuruda, H. Hayakawa, A.  
753 Matsuoka, and L. A. Frank, Quasi-periodic oscillations of the magnetopause during  
754 northward sheath magnetic field, *Geophys. Res. Lett.*, *21*, 2883–2886 (1994).
- 755 Kieokaew, R., B. Lavraud, C. Foullon, S. Toledo-Redondo, N. Fargette, K.-J. Hwang, K. Malakit,  
756 D. Ruffolo, M. Øieroset, T.-D. Phan, et al. Magnetic reconnection inside a flux transfer  
757 event-like structure in magnetopause Kelvin-Helmholtz waves. *Journal of Geophysical*

This is the author's peer reviewed, accepted manuscript. However, the online version of record will be different from this version once it has been copyedited and typeset.

PLEASE CITE THIS ARTICLE AS DOI: 10.1063/1.50067391

Manuscript submitted to Physics of Plasmas

- 758            *Research: Space Physics*, 125, e2019JA027527. <https://doi.org/10.1029/2019JA027527>  
759            (2020).
- 760    Kivelson, M. G., and S.-H. Chen, The magnetopause: Surface waves and instabilities and their  
761            possible dynamic consequences, in *Physics of the Magnetopause, Geophys. Monogr. Ser.*,  
762            vol. 90, edited by P. Song et al., 257 pp., AGU, Washington, D. C (1995).
- 763    Li, W., M. André, Y. V. Khotyaintsev, A. Vaivads, D. B. Graham, S. Toledo-Redondo, C.  
764            Norgren, P. Henri, C. Wang, B. B. Tang, et al., Kinetic evidence of magnetic  
765            reconnection due to Kelvin-Helmholtz waves, *Geophys. Res. Lett.*, **43**, 5635–5643,  
766            doi:10.1002/2016GL069192 (2016).
- 767    Mitchell, D. G., F. Kutchko, D. J. Williams, T. E. Eastman, L. A. Frank and C. T. Russell, An  
768            extended study of the low-latitude boundary layer on the dawn and dusk flank of the  
769            magnetosphere, *J. Geophys. Res.*, 92(A7), 7394– 7404 (1987)
- 770    Miura, A., and P. L. Pritchett, Nonlocal stability analysis of the MHD Kelvin-Helmholtz  
771            instability in a compressible plasma, *J. Geophys. Res.*, **87**, 7431-7444 (1982).
- 772    Moore, T. W., K. Nykyri, and A. P. Dimmock, Cross-scale energy transport in space plasmas,  
773            *Nature Physics*, 12, 1164-1169 (2016)
- 774    Nakamura, T. K. M., M. Fujimoto, and A. Otto, Structure of an MHD-scale Kelvin-Helmholtz  
775            vortex: Two-dimensional two-fluid simulations including finite electron inertial effects,  
776            *Journal of Geophysical Research*, **113**, A09204, doi:10.1029/2007JA012803 (2008).
- 777    Nakamura, T. K. M., W. Daughton, H. Karimabadi, and S. Eriksson, Three-dimensional  
778            dynamics of vortex-induced reconnection and comparison with THEMIS observations,  
779            *Journal of Geophysical Research*, **118**, 5742-5757, doi:10.1002/jgra.50547 (2013).
- 780    Nakamura, T. K. M., and W. Daughton, Turbulent plasma transport across the Earth's low-  
781            latitude boundary layer, *Geophysical Research Letters*, **41**, 8704-8712,  
782            doi:10.1002/2014GL061952 (2014).
- 783    Nakamura, T. K. M., H. Hasegawa, W. Daughton, S. Eriksson, W. Y. Li, and R. Nakamura,  
784            Turbulent mass transfer caused by vortex-induced reconnection in collisionless  
785            magnetospheric plasmas, *Nature Communications*, 8, 1582 (2017a).

This is the author's peer reviewed, accepted manuscript. However, the online version of record will be different from this version once it has been copyedited and typeset.

PLEASE CITE THIS ARTICLE AS DOI: 10.1063/5.0067391

Manuscript submitted to Physics of Plasmas

- 786 Nakamura, T. K. M., Eriksson, S., Hasegawa, H., Zenitani, S., Li, W. Y., Genestreti, K. J.,  
787 Nakamura, R., Daughton, W., Mass and energy transfer across the Earth's magnetopause  
788 caused by vortex-induced reconnection. *Journal of Geophysical Research: Space Physics*,  
789 122, 11,505–11,522. <https://doi.org/10.1002/2017JA024346> (2017b)
- 790 Nakamura, T. K. M., Plaschke, F., Hasegawa, H., Liu, Y.-H., Hwang, K.-J., Blasl, K. A.,  
791 & Nakamura, R. Decay of Kelvin-Helmholtz vortices at the Earth's magnetopause under  
792 pure southward IMF conditions. *Geophysical Research Letters*, 47,  
793 e2020GL087574. <https://doi.org/10.1029/2020GL087574> (2020a).
- 794 Nakamura, T. K. M., Stawarz, J. E., Hasegawa, H., Narita, Y., Franci, L., Wilder, F. D.,  
795 Nakamura, R., Nystrom, W. D., Effects of fluctuating magnetic field on the growth of the  
796 Kelvin-Helmholtz instability at the Earth's magnetopause. *Journal of Geophysical*  
797 *Research: Space Physics*, 125, e2019JA027515, <https://doi.org/10.1029/2019JA027515>  
798 (2020b).
- 799 Nakamura, T.K.M.. The Earth's Low-Latitude Boundary Layer, *In Magnetospheres in the Solar*  
800 *System* (eds R. Maggiolo, N. André, H. Hasegawa, D.T. Welling, Y. Zhang and L.J.  
801 Paxton), Wiley, <https://doi.org/10.1002/9781119815624.ch12>, (2021).
- 802 Nakamura, T.K.M (2021): This is the data set. Zenodo. <http://doi.org/10.5281/zenodo.5725490>.
- 803 Panov, E. V., A. V. Artemyev, R. Nakamura, and W. Baumjohann, Two types of tangential  
804 magnetopause current sheets: Cluster observations and theory, *J. Geophys. Res.*, 116,  
805 A12204, doi:10.1029/2011JA016860 (2011).
- 806 Palmroth, M., U., Ganse, Y., Pfau-Kempf, M. Battarbee, L. Turc, T. Brito, M. Grandin, S.  
807 Hoilijoki, A. Sandroos & S. von Alfthan, Vlasov methods in space physics and  
808 astrophysics, *Living Rev. Comput. Astrophys.* 4, 1, [https://doi.org/10.1007/s41115-](https://doi.org/10.1007/s41115-018-0003-2)  
809 [018-0003-2](https://doi.org/10.1007/s41115-018-0003-2) (2018).
- 810 Sckopke, N. G., G. Paschmann, G. Haerendel, B. U. O. Sonnerup, S. J. Bame, T. G. Forbes,  
811 E.W. Hones Jr., and C. T. Russell, Structure of the lowlatitude boundary layer, *J.*  
812 *Geophys. Res.*, 86, 2099–2110 (1981).

This is the author's peer reviewed, accepted manuscript. However, the online version of record will be different from this version once it has been copyedited and typeset.

PLEASE CITE THIS ARTICLE AS DOI: 10.1063/1.50067391

Manuscript submitted to Physics of Plasmas

813 Slinker, S. P., J. A. Fedder, D. G. Sibeck, J. G. Lyon, L. A. Frank, and T. Mukai, Simulation of  
 814 magnetopause oscillations observed January 9, 1996, *Geophys. Res. Lett.* 30(11), 1569,  
 815 doi:10.1029/2003GL017063 (2003).

816 Stawarz, J. E., S. Eriksson, F. D. Wilder, R. E. Ergun, S. J. Schwartz, A. Pouquet, J. L. Burch,  
 817 B. L. Giles, Y. Khotyaintsev, O. Le Contel, et al., Observations of turbulence in a Kelvin-  
 818 Helmholtz event on 8 September 2015 by the Magnetospheric Multiscale mission, *J.*  
 819 *Geophys. Res. Space Physics*, 121, 11,021–11,034, doi:10.1002/2016JA023458 (2016).

820 Tang, B., Li, W., Wang, C., Dai, L., Khotyaintsev, Y., Lindqvist, P.-A., Ergun, R., Le Contel, O.,  
 821 Pollock, C., Russell, C., and Burch, J., Magnetic depression and electron transport in an  
 822 ion-scale flux rope associated with Kelvin–Helmholtz waves, *Ann. Geophys.*, 36, 879-  
 823 889, <https://doi.org/10.5194/angeo-36-879-2018> (2018).

824 Umeda, T., T.K.M. Nakamura, Electromagnetic linear dispersion relation for plasma with a drift  
 825 across magnetic field revisited, *Phys. Plasmas*, 25, 102109, doi:10.1063/1.5050542  
 826 (2018).

827 Vernisse, Y. B. Lavraud, S. Eriksson, D. J. Gershman, J. Dorelli, C. Pollock, B. Giles, N. Aunai,  
 828 L. Avakov, J. Burch, et al., Signatures of complex magnetic topologies from multiple  
 829 reconnection sites induced by Kelvin-Helmholtz instability, *Journal of Geophysical*  
 830 *Research*, doi:10.1002/2016JA023051 (2016).

831  
 832  
 833



This is the author's peer reviewed, accepted manuscript. However, the online version of record will be different from this version once it has been copyedited and typeset.

PLEASE CITE THIS ARTICLE AS DOI: 10.1063/1.50067391

Manuscript submitted to Physics of Plasmas

834 **TABLE I.** Key differences among simulation runs employed in this paper.

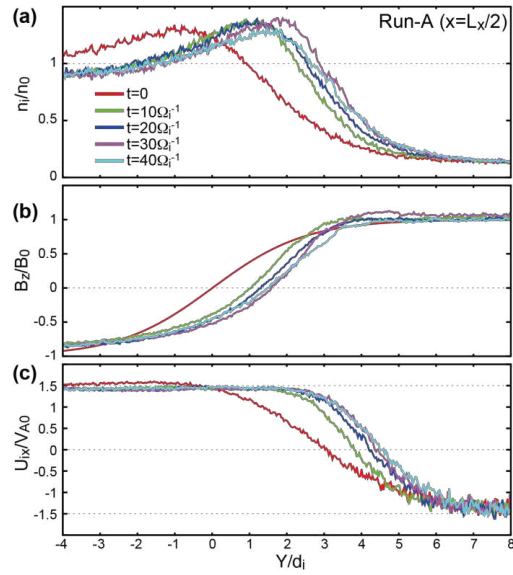
Run	A	B	C	D
2D or 3D	2D	3D	2D	2D
System size ( $d_i$ )	100×100	15×30×10.4	15×30	15×30
In-plane field ( $B_0$ )	$B_{x10}:0.2$ $B_{x20}:0.0$	$B_{x10}:0.17$ $B_{x20}:0.17$	$B_{x10}:0.17$ $B_{x20}:0.17$	$B_{x10}:0.0$ $B_{x20}:0.0$
Potential 2ndary processes	RTI LHDI	RTI LHDI Reconnection	RTI	RTI LHDI

835

This is the author's peer reviewed, accepted manuscript. However, the online version of record will be different from this version once it has been copyedited and typeset.

PLEASE CITE THIS ARTICLE AS DOI: 10.1063/1.50067391

Manuscript submitted to Physics of Plasmas



836

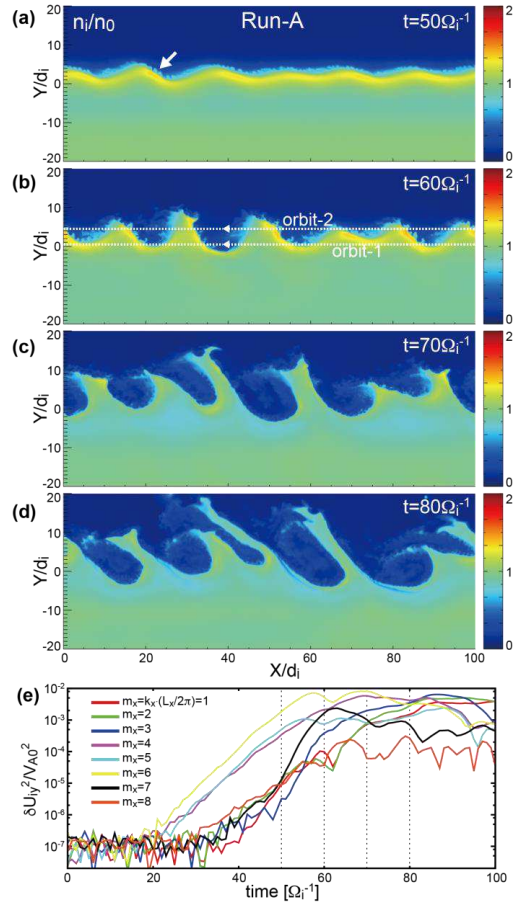
837 **FIGURE 1.** Time evolution of the profiles in the y-direction at  $x=L_x/2$  for the large-scale 2D run  
 838 (Run-A) of (a) the ion density  $n_i$ , (b) the out-of-plane component of the magnetic field  $B_z$ , and (c)  
 839 the x-component of the ion bulk velocity  $U_{ix}$  from  $t=0$  to  $40\Omega_i^{-1}$ .

840

This is the author's peer reviewed, accepted manuscript. However, the online version of record will be different from this version once it has been copyedited and typeset.

PLEASE CITE THIS ARTICLE AS DOI: 10.1063/5.0067391

Manuscript submitted to Physics of Plasmas



841

842 **FIGURE 2.** (a-d) Time evolution of color contours of  $n_i$  in the  $x$ - $y$  plane from  $t=50$  to  $80 \Omega_i^{-1}$  for

843 Run-A. (e) Time evolution of the 1-D power spectra ( $k_x$ ) of  $U_{iy}$  modes ( $m_x=1$  to  $m_x=8$ ) around

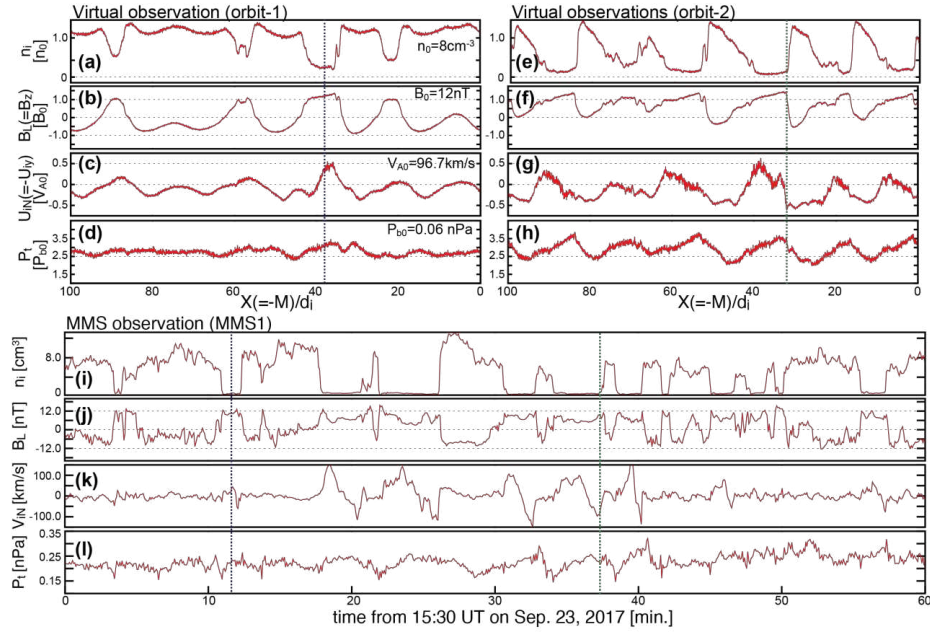
844 the center of the boundary ( $y=0\pm 8.3d_i$ ). Vertical lines indicate the times shown in Figs. 2a-2d.

845

This is the author's peer reviewed, accepted manuscript. However, the online version of record will be different from this version once it has been copyedited and typeset.

PLEASE CITE THIS ARTICLE AS DOI: 10.1063/5.0067391

Manuscript submitted to Physics of Plasmas



846

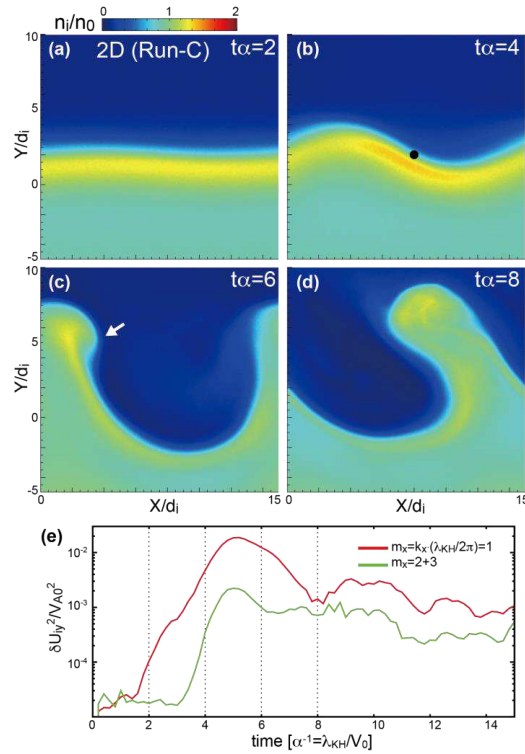
847 **FIGURE 3.** (a-h) Virtual observations of the KH waves for Run-A, made along the orbits-1 and  
 848 2 shown in Fig. 2b and (i-l) the in-situ observations by the MMS1 spacecraft for 1 hour from  
 849 15:30UT of the ion density, L (=z) component of the magnetic field, N (=y) component of the  
 850 ion bulk velocity and the total pressure. The time interval in Figs. 3i-3l is the same as the one in  
 851 Fig. 3 in B21.

852

This is the author's peer reviewed, accepted manuscript. However, the online version of record will be different from this version once it has been copyedited and typeset.

PLEASE CITE THIS ARTICLE AS DOI: 10.1063/5.0067391

Manuscript submitted to Physics of Plasmas



853

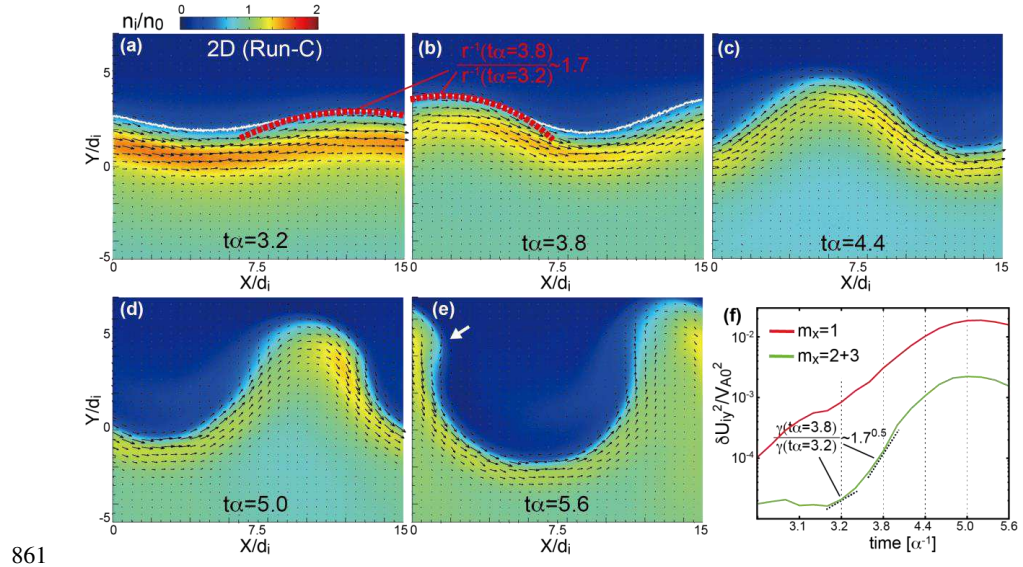
854 **FIGURE 4.** (a-d) Time evolution of color contours in the  $x$ - $y$  plane of  $n_i$  from  $t=2$  to  $8\alpha^{-1}$  for the  
 855 local 2D run (Run-C), where  $\alpha^{-1} = \lambda_{KH}/V_0$  is the time unit for the growth phase of the KHI  
 856 (Nakamura et al., 2013). (e) Time evolution of the 1-D power spectra ( $k_x$ ) of  $U_{iy}$  modes ( $m_x=1$   
 857 and  $m_x=2+3$ ) obtained by calculating the power of each mode at each  $y$  and then picking up the  
 858 maximum value for each mode. Vertical dotted lines in Fig. 4e indicate the times in Figs.  
 859 4a-4d.

860

This is the author's peer reviewed, accepted manuscript. However, the online version of record will be different from this version once it has been copyedited and typeset.

PLEASE CITE THIS ARTICLE AS DOI: 10.1063/5.0067391

Manuscript submitted to Physics of Plasmas



861

862 **FIGURE 5.** (a-e) Time evolution of  $n_i$  contours for Run-C from  $t=3.2$  to  $5.6\alpha^{-1}$ . Arrows show  
 863 the in-plane components of the current density. The white and red dashed curves in Figs. 5a and  
 864 5b show the density surface with  $(n_{10}+n_{20})/2$  and a portion of the fitted circles near the top of the  
 865 primary wave structures, respectively.  $r$  in Figs. 5a and 5b indicate the curvature radius for the  
 866 yellow curves. (f) Time evolution of the 1-D power spectra ( $k_x$ ) of  $U_{iy}$  modes  $m_x=1$  and  $m_x=2+3$ .  
 867 Vertical lines indicate the times shown in Figs. 5a-5e.

868

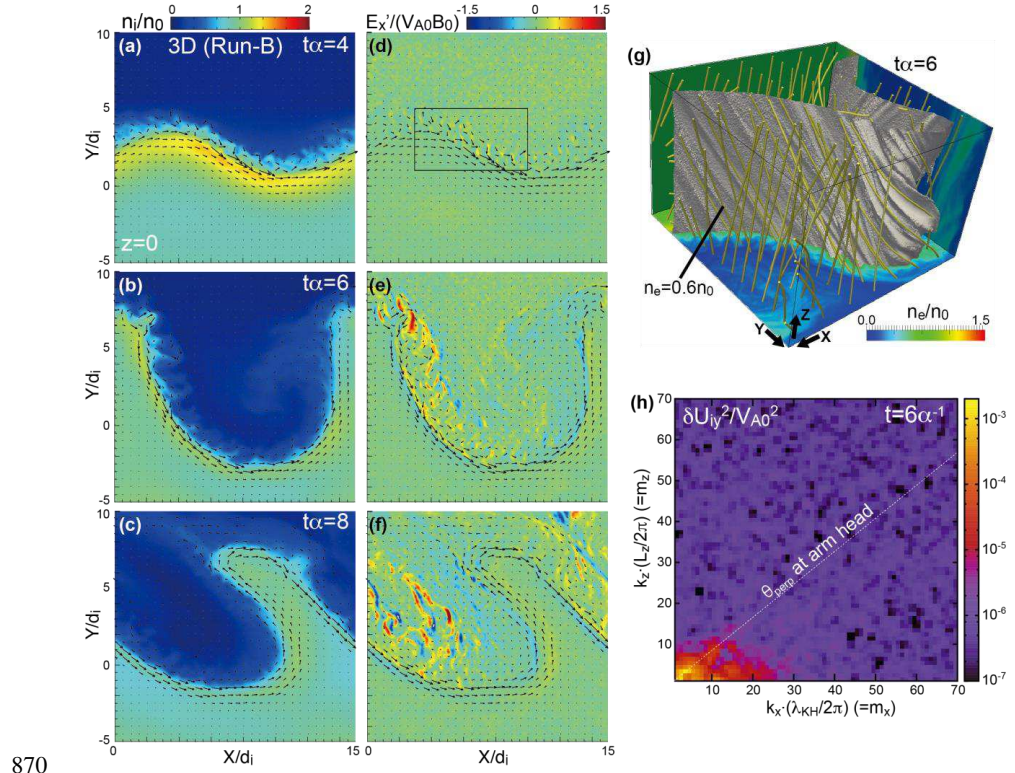
869



This is the author's peer reviewed, accepted manuscript. However, the online version of record will be different from this version once it has been copyedited and typeset.

PLEASE CITE THIS ARTICLE AS DOI: 10.1063/1.50067391

Manuscript submitted to Physics of Plasmas



870

871 **FIGURE 6.** (a-f) Time evolution of color contours of  $n_i$  (left) and the x-component of the  
 872 electric field in the electron frame  $E_x' = (\mathbf{E} + \mathbf{U}_e \times \mathbf{B})_x$  (right) from  $t=2$  to  $8\alpha^{-1}$  (the same time  
 873 interval as Fig. 4) for the local 3D run (Run-B) at  $z=0$ . Arrows show the in-plane components of  
 874 the current density. (g) 3D view of the electron density surface of  $n_e=0.6n_0$  at  $t=6\alpha^{-1}$  for Run-B  
 875 with the electron density contours in the  $x$ - $y$  plane at  $z=0$ ,  $x$ - $z$  plane at  $y=0$  and  $y$ - $z$  plane at  $x=0$   
 876 and randomly distributed magnetic field lines. (h) 2-D power spectra ( $k_x, k_z$ ) of  $U_{iy}$  at  $t=6\alpha^{-1}$   
 877 around the center of the boundary ( $y=0 \pm 5d_i$ ) for Run-B. The dotted line indicates the angle of the  
 878 perpendicular direction to the magnetic field in the  $x$ - $z$  plane  $\theta_{\text{perp}}$  at the head of the high-density  
 879 arm.

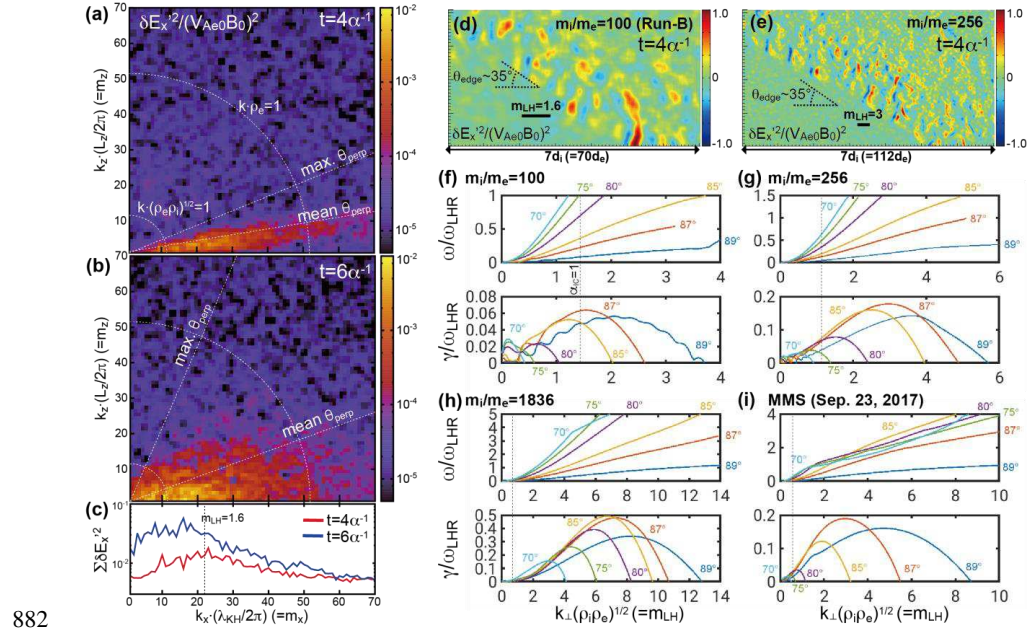
880

881

This is the author's peer reviewed, accepted manuscript. However, the online version of record will be different from this version once it has been copyedited and typeset.

PLEASE CITE THIS ARTICLE AS DOI: 10.1063/5.0067391

Manuscript submitted to Physics of Plasmas



882

883 **FIGURE 7.** (a-c) 2-D power spectra ( $k_x, k_z$ ) of  $E_x'$  and sum of the spectra in  $k_z$  at  $t=4$  and  $6\alpha^{-1}$   
 884 around the center of the boundary ( $y=0\pm 5d_i$ ) for Run-B. The dotted lines in Figs. 7a and 7b  
 885 indicate the angle of the perpendicular direction to the magnetic field in the  $x$ - $z$  plane  $\theta_{\text{perp}}$  at the  
 886 head of the high-density arm, the maximum and mean  $\theta_{\text{perp}}$  on the low-density side of the density  
 887 gradient layer defined as the region with  $0.2 < n_e/n_0 < 0.4$ , and the wavelengths for  $k_{\perp}\rho_e = 1$  and  
 888  $k_{\perp}(\rho_i\rho_e)^{1/2} = 1$ . (d) The zoomed-in view of the  $E_x'$  contour in the region marked in Fig. 6d. (e)  
 889 The same as Fig. 7d, but for an additional run with  $m_i/m_e=256$ . (f-i) Linear dispersion relations at  
 890 the edge of the KH waves derived by Umeda & Nakamura (2018). Panels show wave modes  
 891 with wave normal angles quasi-perpendicular to the ambient magnetic field ( $\phi = 70^\circ - 89^\circ$ ) for  
 892 parameters, obtained from the simulation near the compressed density gradient layer at  $t=4\alpha^{-1}$   
 893 marked in Fig. 4b (f), similar to Fig. 7f but for  $m_i/m_e=256$  (g) and  $m_i/m_e=1836$  (h), and obtained  
 894 from the MMS observations on September 23, 2017 (B21).

895

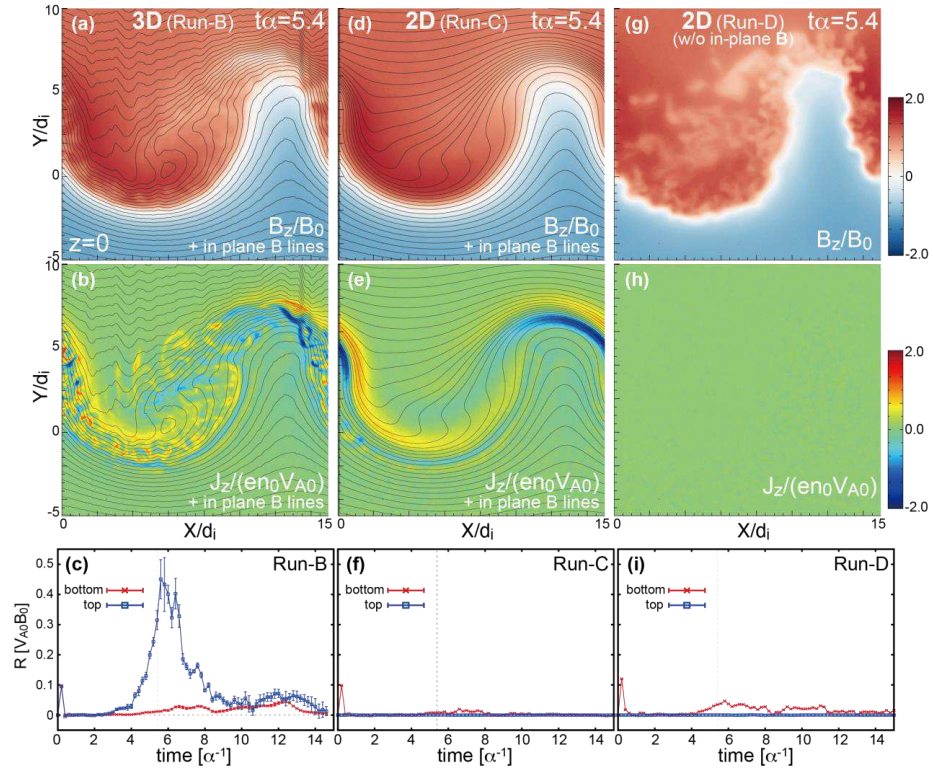


This is the author's peer reviewed, accepted manuscript. However, the online version of record will be different from this version once it has been copyedited and typeset.

PLEASE CITE THIS ARTICLE AS DOI: 10.1063/5.0067391

Manuscript submitted to Physics of Plasmas

896



897

898 **FIGURE 8.** (top and middle) Color contours of  $B_z$  and  $J_z$  at  $t=5.4\alpha^{-1}$  in the  $x$ - $y$  plane ( $z=0$  for the  
 899 3-D run), and (bottom) time evolutions of the normalized, global reconnection rate  $R$  (Daughton  
 900 et al., 2014) computed from the integrated magnetic flux that crosses the mixing surfaces,  
 901 defined as  $|F_e| = 0.99$ , on the low-density and positive- $B_z$  (top) and high-density and negative- $B_z$   
 902 (bottom) sides for Runs-B-D. Here  $F_e=(n_{e1}-n_{e2})/(n_{e1}+n_{e2})$  is the mixing measure. The black  
 903 curves for Runs-B and C show the surfaces of the  $z$ -component of the vector potential  
 904 corresponding to the in-plane magnetic field lines in 2-D. The vertical lines in the bottom plots  
 905 indicate the time shown in the top plots.

906

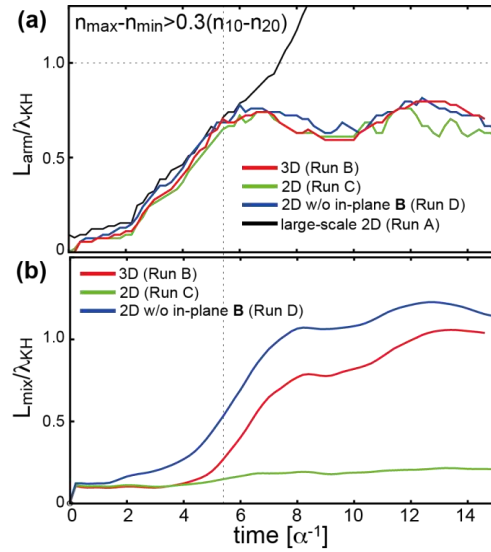
37

This is the author's peer reviewed, accepted manuscript. However, the online version of record will be different from this version once it has been copyedited and typeset.

PLEASE CITE THIS ARTICLE AS DOI: 10.1063/5.0067391

Manuscript submitted to Physics of Plasmas

907



908

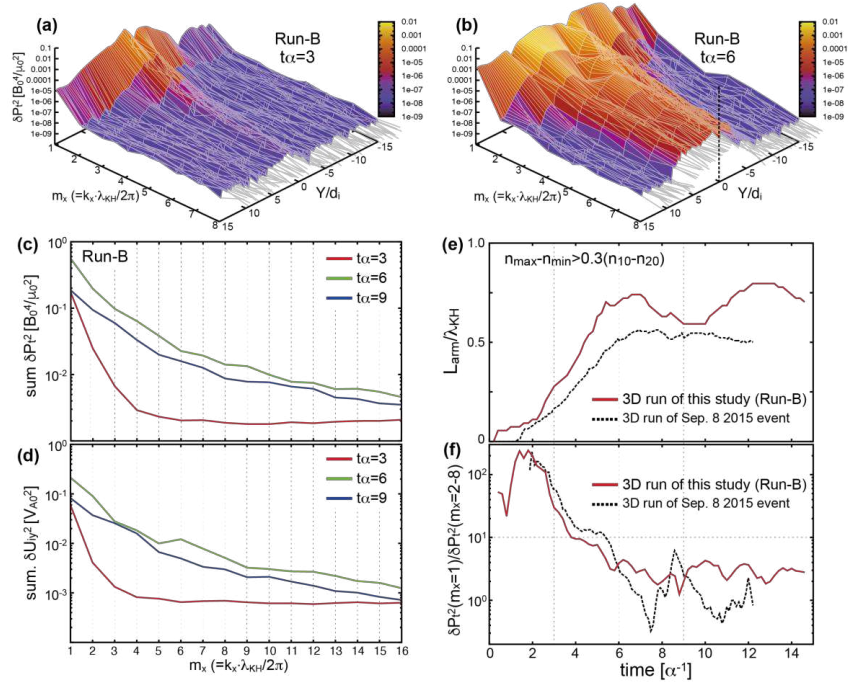
909 **FIGURE 9.** Time evolutions of (a) the length in the boundary normal (y) direction of the region  
 910 with the large-scale density fluctuations (i.e., the high-density arm), defined as the region where  
 911 the profile in the x-direction contains the density variation larger than  $0.3(n_{10}-n_{20})$ , and (b) the  
 912 averaged thickness in y of the mixing region with  $|F_e| < 0.99$  for Runs B-D. The black curve in  
 913 Fig. 9a shows the result from Run-A in which the normalized units  $\lambda_{\text{KH}}$  and  $\alpha^{-1} = \lambda_{\text{KH}}/V_0$  are  
 914 employed for the fastest growing mode  $m_x = 6$ . The vertical lines in Fig. 9a and 9b indicate the  
 915 time shown in Fig. 8.

916

This is the author's peer reviewed, accepted manuscript. However, the online version of record will be different from this version once it has been copyedited and typeset.

PLEASE CITE THIS ARTICLE AS DOI: 10.1063/5.0067391

Manuscript submitted to Physics of Plasmas



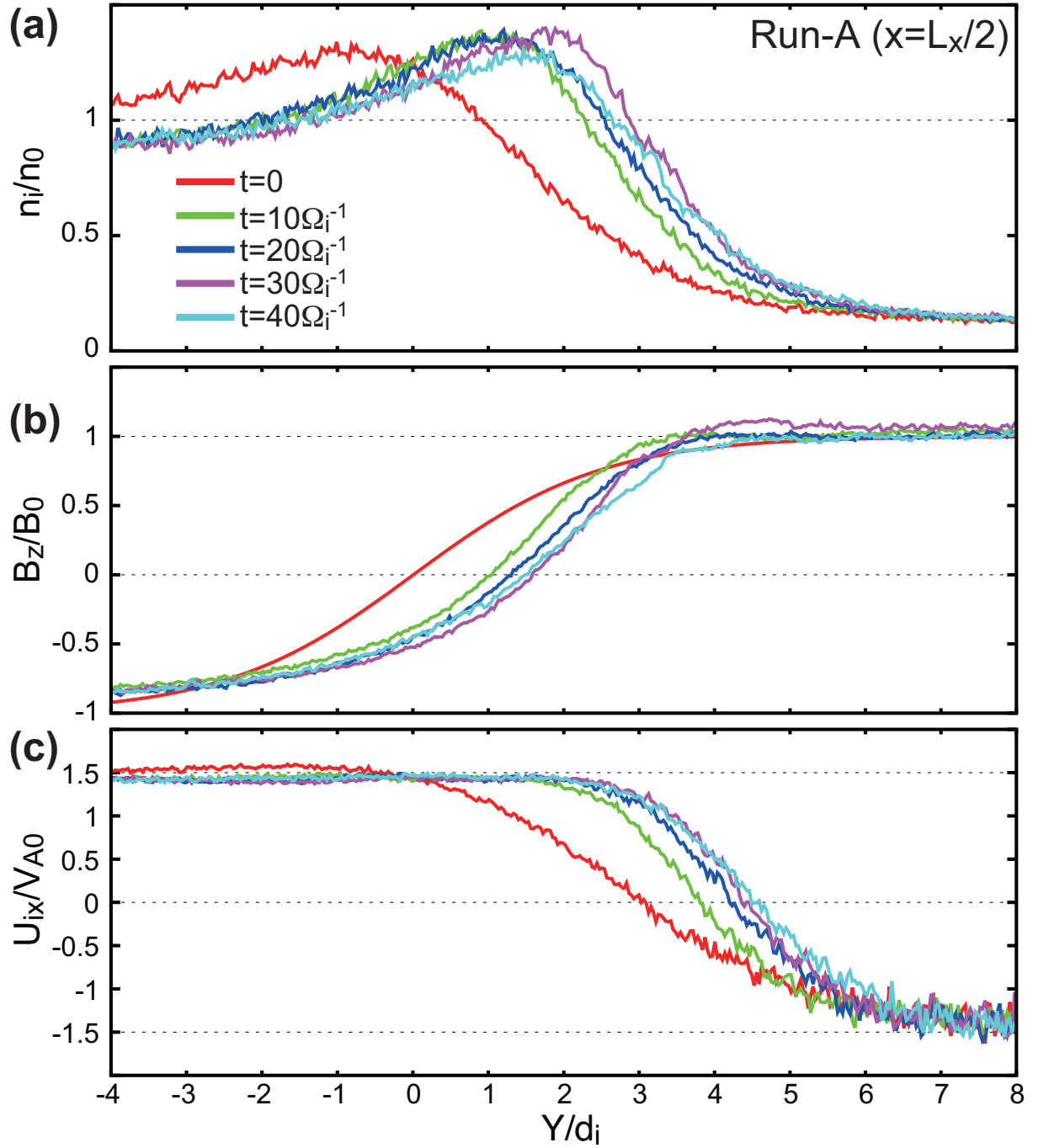
917

918 **FIGURE 10.** (a,b) 1-D power spectra ( $k_x$ ) for Run-B of the total pressure  $P_t$  for each  $y$  averaged  
 919 in  $z$  at  $t=3\alpha^{-1}$  (linear phase) and  $t=6\alpha^{-1}$  (early non-linear phase). (c, d) The same spectra as Figs.  
 920 10a and 10b but integrated in  $y$  of (c)  $P_t$  and (d)  $U_{iy}$  at  $t=3, 6$  and  $9\alpha^{-1}$ . (e, f) Time evolution for  
 921 Run-B of (e) the thickness of the region with the large-scale density fluctuations (the same as the  
 922 red curve in Fig. 9a), and (f) the ratio of the  $P_t$  power between  $m_x=1$  and  $m_x=2-8$  within the  
 923 region having the moderate density fluctuations. The black dashed curves in Figs. 10e and 10f  
 924 show the results calculated from the 3D run of the September 8 2015 event employed in  
 925 Nakamura (2021), in which the KH waves were observed during northward IMF.

926

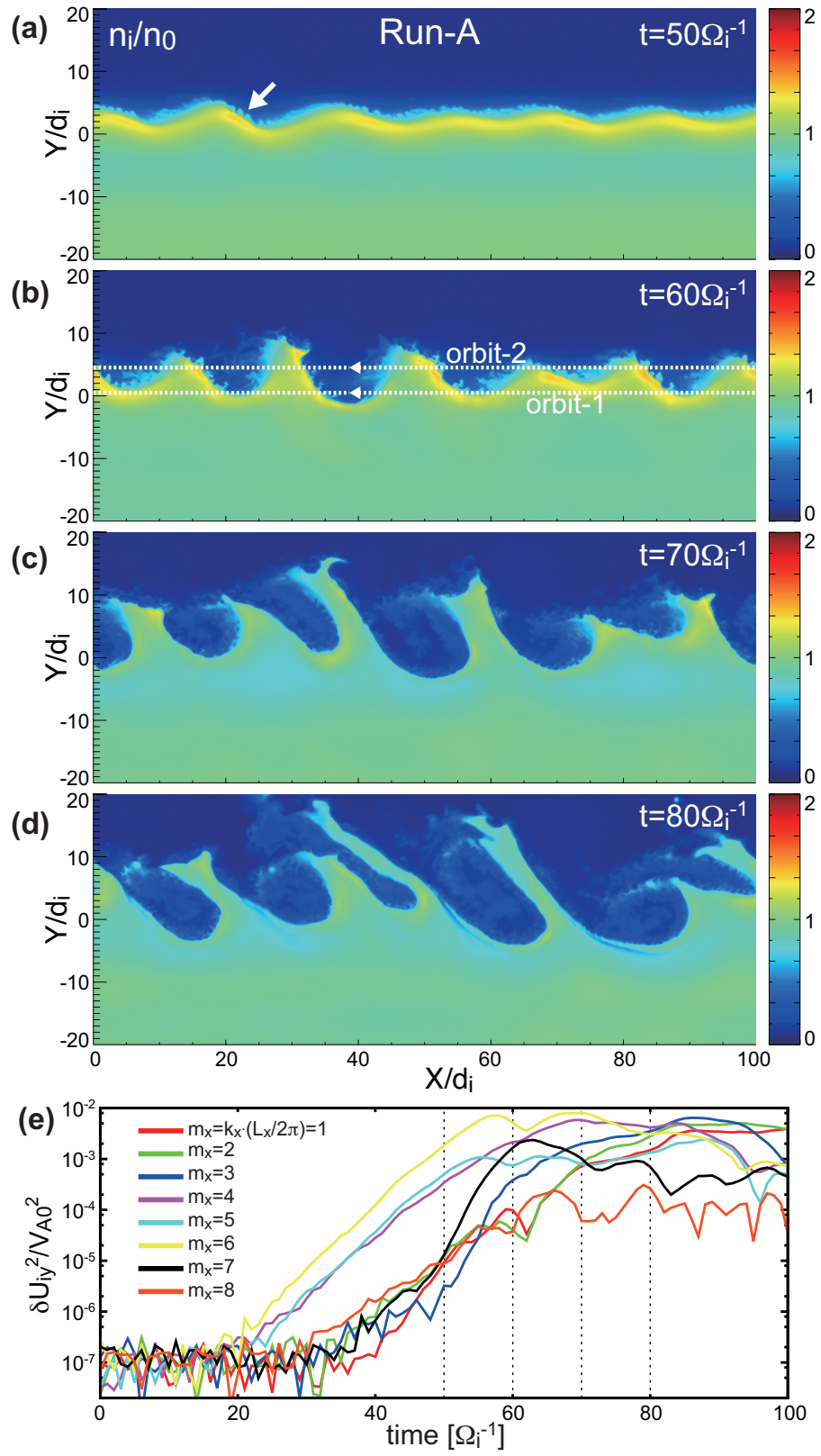
This is the author's peer reviewed, accepted manuscript. However, the online version of record will be different from this version once it has been copyedited and typeset.

PLEASE CITE THIS ARTICLE AS DOI: 10.1063/1.50067391



This is the author's peer reviewed, accepted manuscript. However, the online version of record will be different from this version once it has been copyedited and typeset.

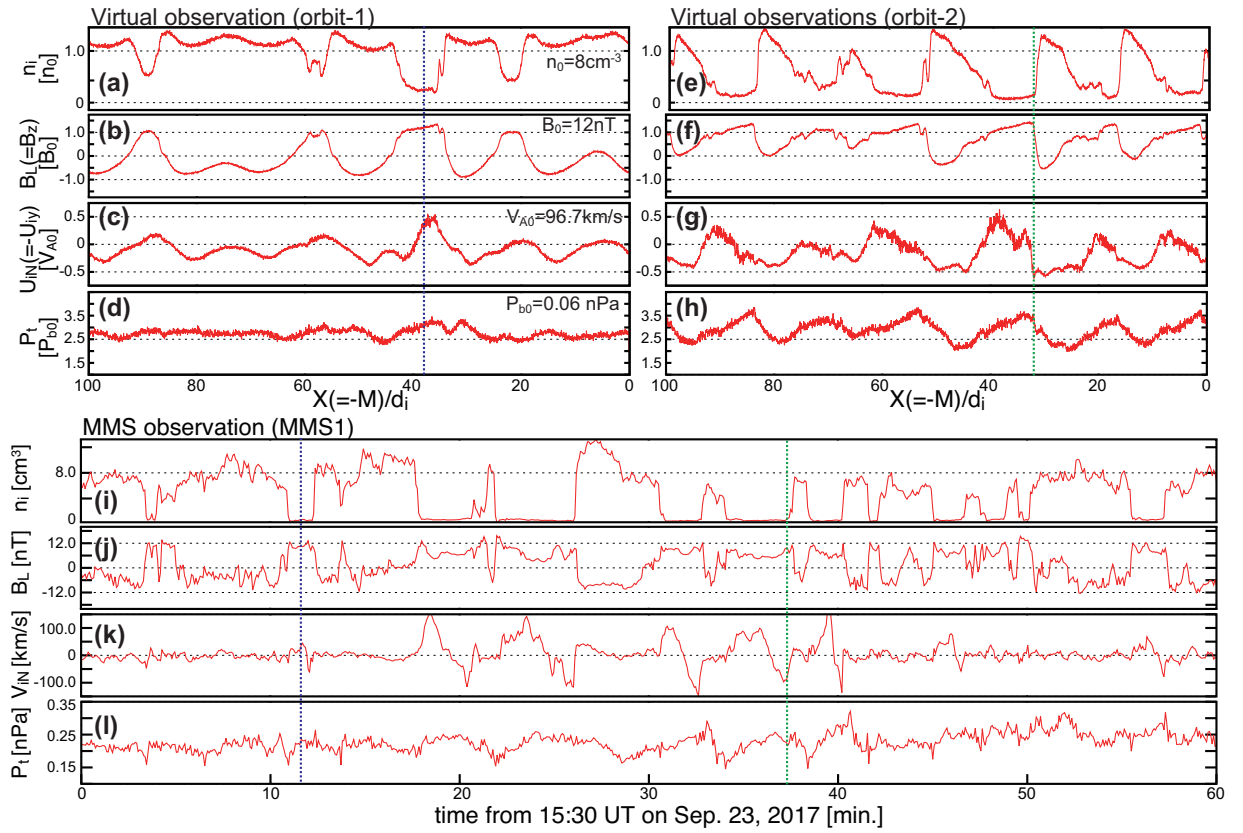
PLEASE CITE THIS ARTICLE AS DOI: 10.1063/5.0067391





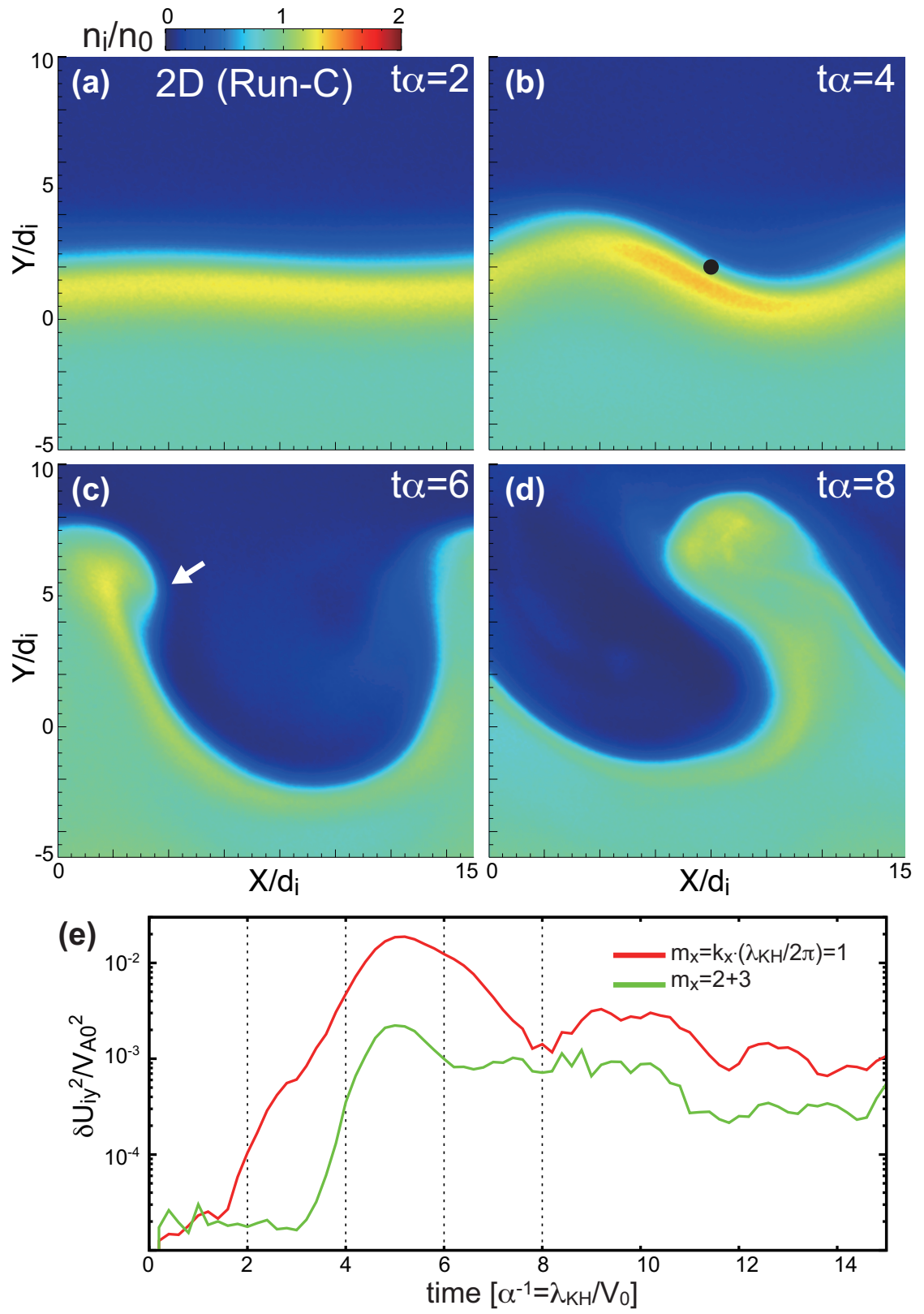
This is the author's peer reviewed, accepted manuscript. However, the online version of record will be different from this version once it has been copyedited and typeset.

PLEASE CITE THIS ARTICLE AS DOI: 10.1063/1.50067391



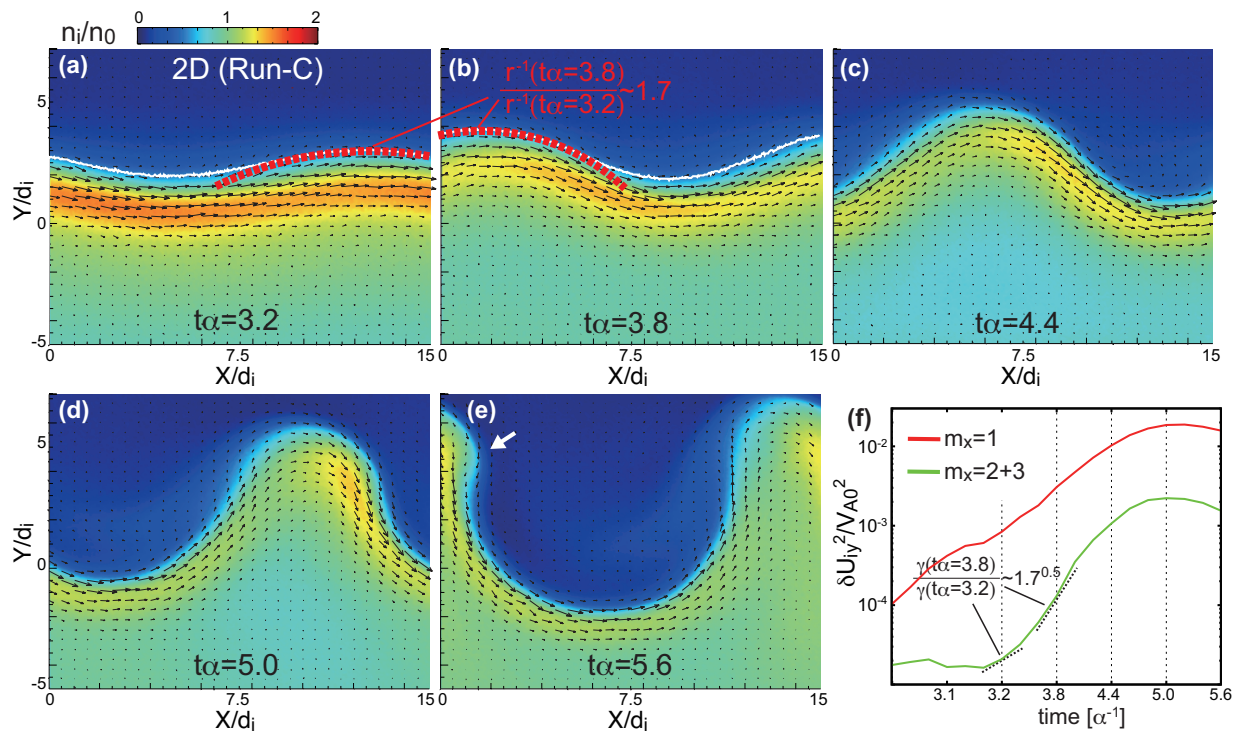
This is the author's peer reviewed, accepted manuscript. However, the online version of record will be different from this version once it has been copyedited and typeset.

PLEASE CITE THIS ARTICLE AS DOI: 10.1063/5.0067391



This is the author's peer reviewed, accepted manuscript. However, the online version of record will be different from this version once it has been copyedited and typeset.

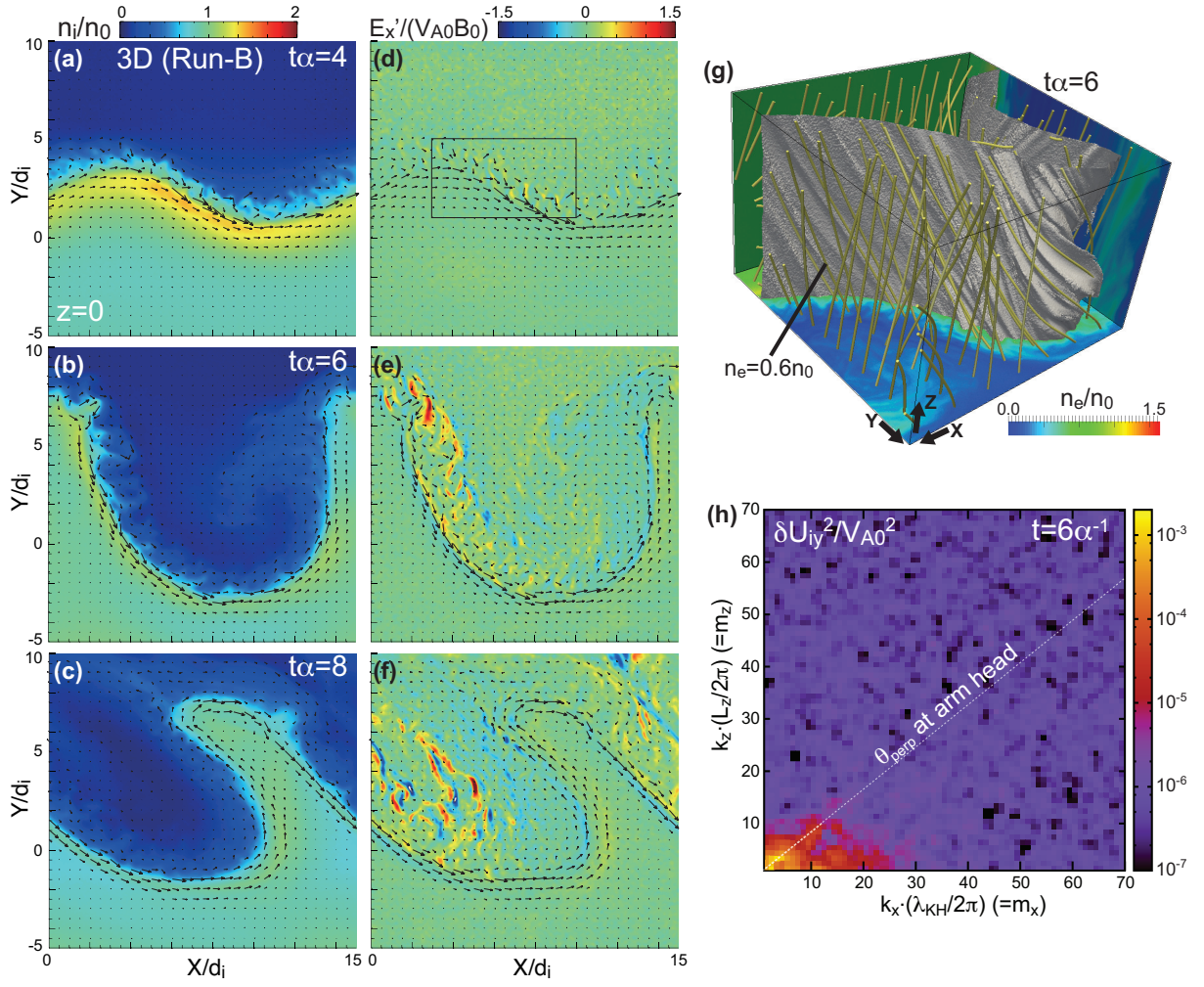
PLEASE CITE THIS ARTICLE AS DOI: 10.1063/5.0067391





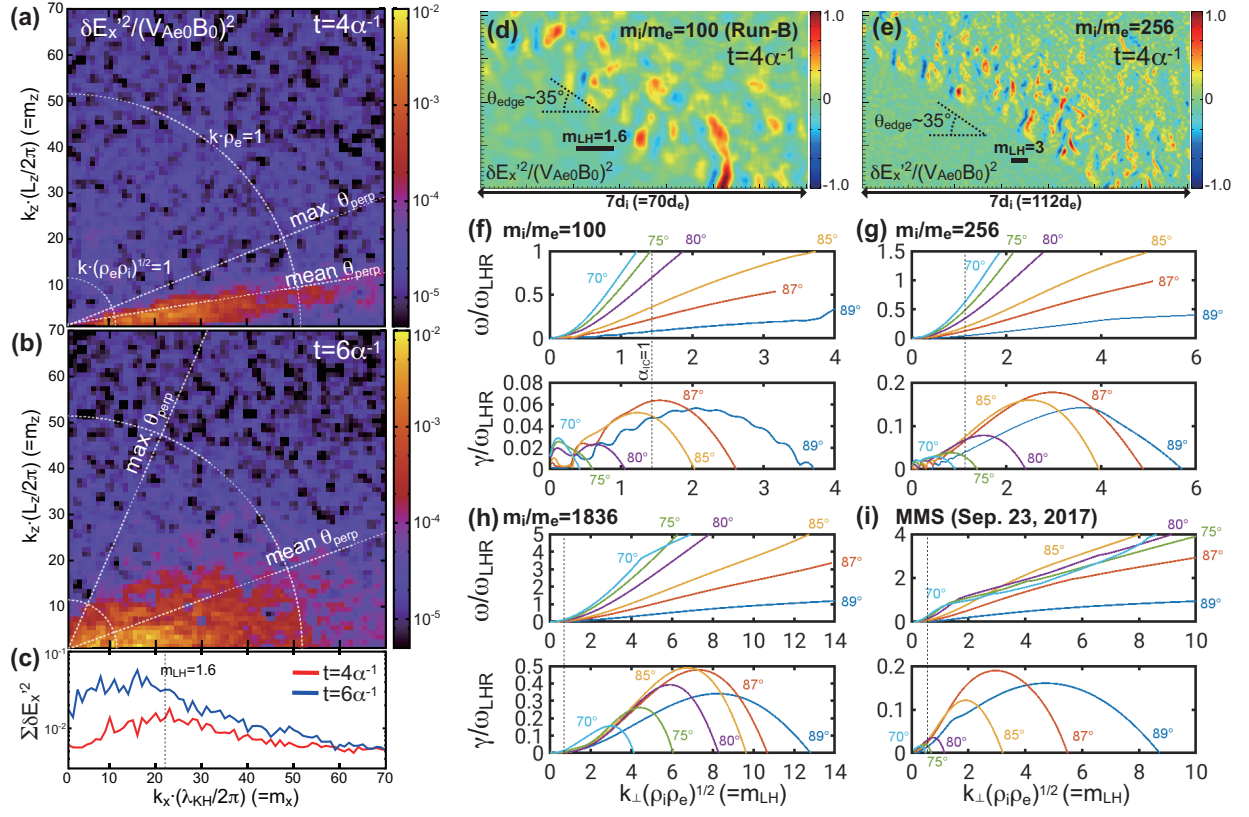
This is the author's peer reviewed, accepted manuscript. However, the online version of record will be different from this version once it has been copyedited and typeset.

PLEASE CITE THIS ARTICLE AS DOI: 10.1063/5.0067391



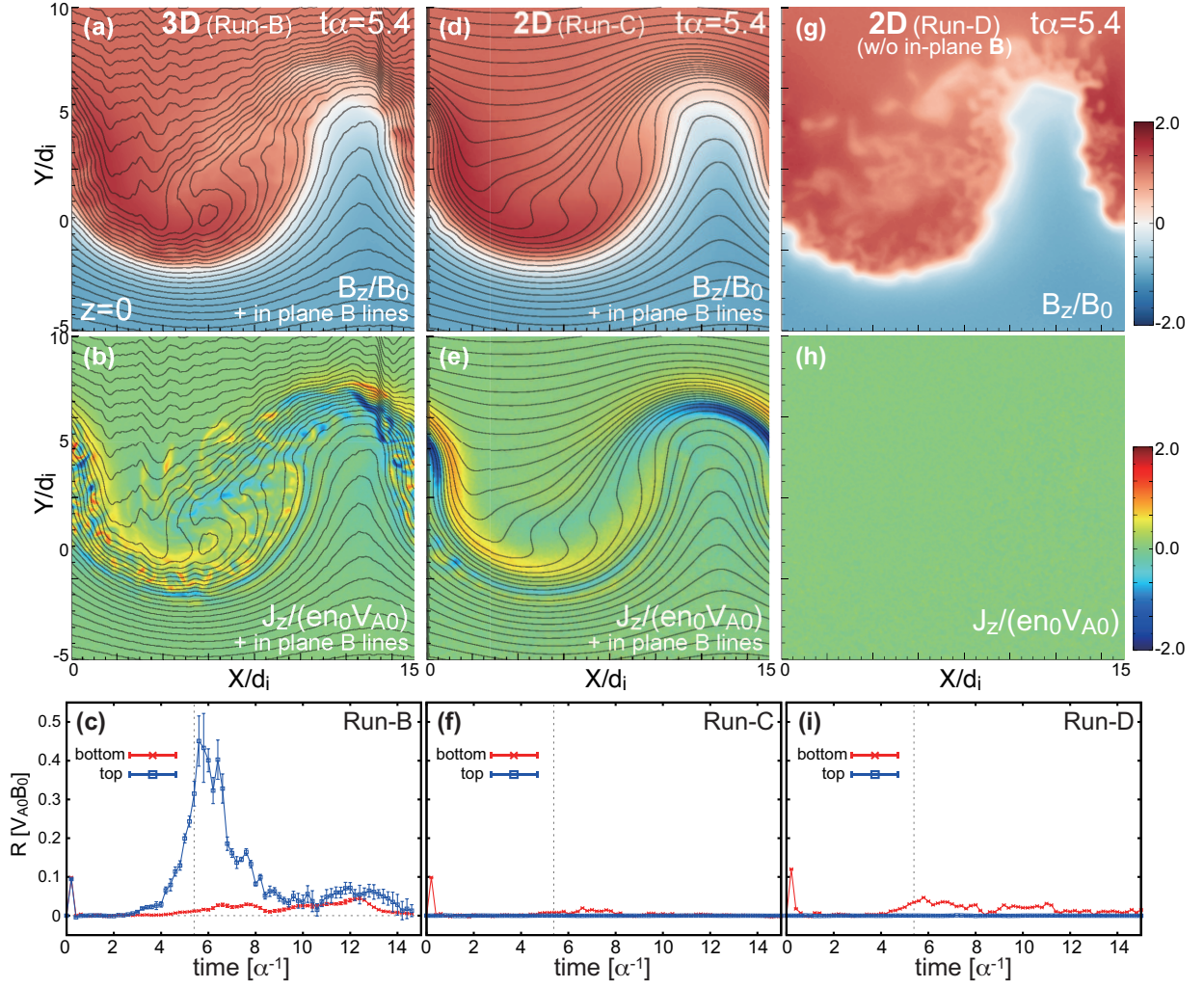
This is the author's peer reviewed, accepted manuscript. However, the online version of record will be different from this version once it has been copyedited and typeset.

PLEASE CITE THIS ARTICLE AS DOI: 10.1063/5.0067391



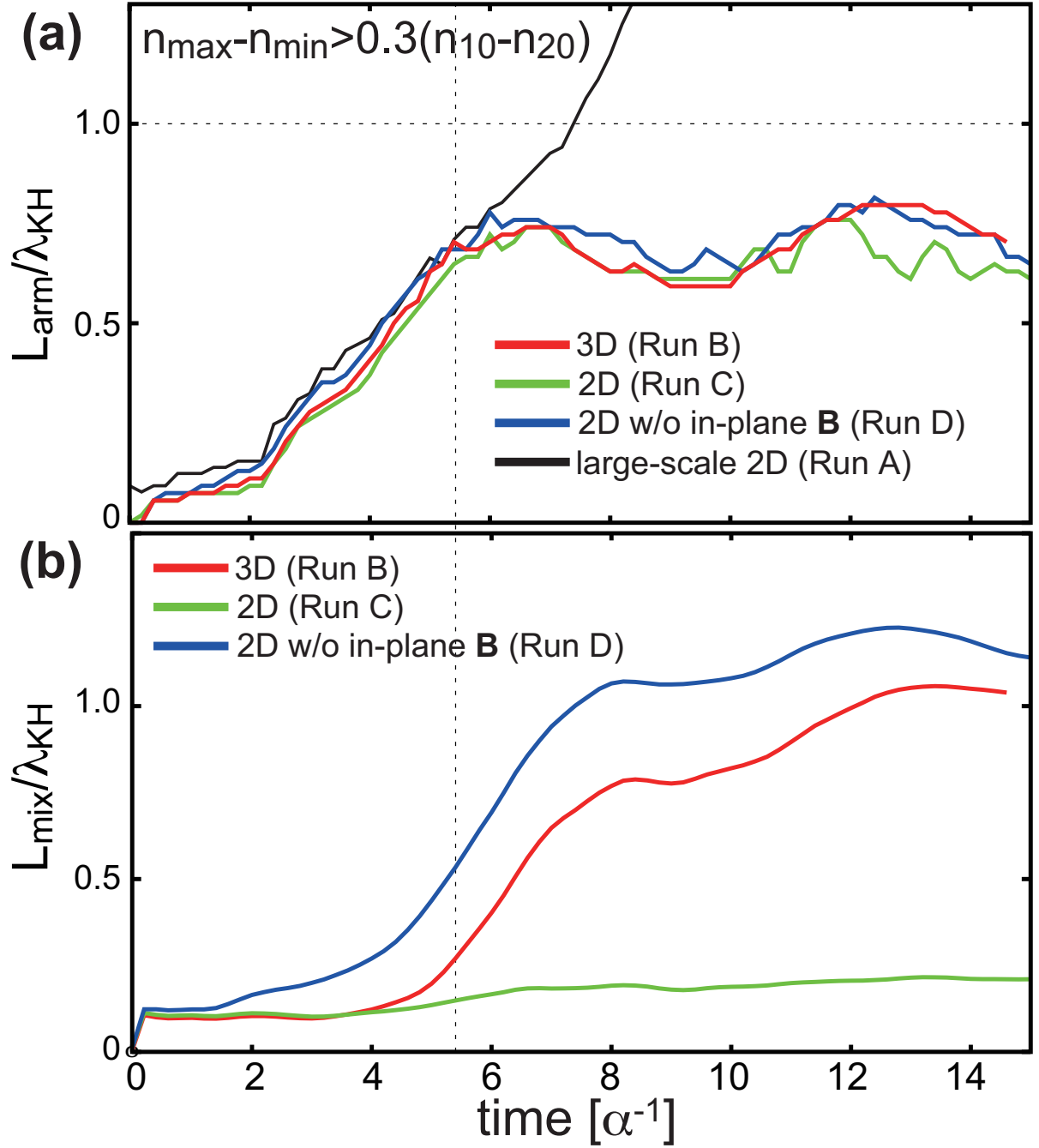
This is the author's peer reviewed, accepted manuscript. However, the online version of record will be different from this version once it has been copyedited and typeset.

PLEASE CITE THIS ARTICLE AS DOI: 10.1063/5.0067391



This is the author's peer reviewed, accepted manuscript. However, the online version of record will be different from this version once it has been copyedited and typeset.

PLEASE CITE THIS ARTICLE AS DOI: 10.1063/5.0067391





This is the author's peer reviewed, accepted manuscript. However, the online version of record will be different from this version once it has been copyedited and typeset.

PLEASE CITE THIS ARTICLE AS DOI: 10.1063/5.0067391

